The Astrophysical Journal, 745:63 (23pp), 2012 January 20 doi:10.1088/0004-637X/745/1/63

DIFFUSIVE ACCELERATION OF PARTICLES AT OBLIQUE, RELATIVISTIC, MAGNETOHYDRODYNAMIC SHOCKS

Errol J. Summerlin[1] and Matthew G. Baring[2]
[1] Heliospheric Physics Laboratory, Code 672, NASA's Goddard Space Flight Center, Greenbelt, MD 20770, USA; errol.summerlin@nasa.gov
[2] Department of Physics and Astronomy, MS 108, Rice University, Houston, TX 77251, USA; baring@rice.edu
Received 2011 August 9; accepted 2011 October 24; published 2011 December 29

ABSTRACT

Diffusive shock acceleration (DSA) at relativistic shocks is expected to be an important acceleration mechanism in a variety of astrophysical objects including extragalactic jets in active galactic nuclei and gamma-ray bursts. These sources remain good candidate sites for the generation of ultrahigh energy cosmic rays. In this paper, key predictions of DSA at relativistic shocks that are germane to the production of relativistic electrons and ions are outlined. The technique employed to identify these characteristics is a Monte Carlo simulation of such diffusive acceleration in test-particle, relativistic, oblique, magnetohydrodynamic (MHD) shocks. Using a compact prescription for diffusion of charges in MHD turbulence, this approach generates particle angular and momentum distributions at any position upstream or downstream of the shock. Simulation output is presented for both small angle and large angle scattering scenarios, and a variety of shock obliquities including superluminal regimes when the de Hoffmann–Teller frame does not exist. The distribution function power-law indices compare favorably with results from other techniques. They are found to depend sensitively on the mean magnetic field orientation in the shock, and the nature of MHD turbulence that propagates along fields in shock environs. An interesting regime of flat-spectrum generation is addressed; we provide evidence for it being due to shock drift acceleration, a phenomenon well known in heliospheric shock studies. The impact of these theoretical results on blazar science is outlined. Specifically, *Fermi* Large Area Telescope gamma-ray observations of these relativistic jet sources are providing significant constraints on important environmental quantities for relativistic shocks, namely, the field obliquity, the frequency of scattering, and the level of field turbulence.

Key words: acceleration of particles – cosmic rays – gamma-ray burst: general – magnetohydrodynamics (MHD) – shock waves

Online-only material: color figures

1. INTRODUCTION

Collisionless magnetohydrodynamic (MHD) shocks are found in diverse environments ranging from the inner heliosphere to the central regions of distant galaxies and other astrophysical objects. Particle acceleration at these collisionless shocks is believed to be a common phenomenon in space plasmas. In the heliosphere, direct measurements of accelerated non-thermal ions and electrons in various energy ranges at Earth's bow shock (e.g., Scholer et al. 1980; Möbius et al. 1987; Gosling et al. 1989) and interplanetary shocks (e.g., Sarris & Van Allen 1974; Decker et al. 1981; Tan et al. 1988; Baring et al. 1997) indicate energization processes that are intimately connected to shock environs. Outside the heliosphere, non-thermal particle distributions are inferred from observed photon spectra of supernova remnants, pulsar wind nebulae, blazars, and gamma-ray bursts (GRBs; e.g., Blandford & Eichler 1987 and references therein), all of which possess supersonic outflows that are readily shocked. Commonly, these non-thermal distributions take the form of power-law tails that can extend to thousands or millions of times the ambient thermal energies of the particles.

First-order Fermi acceleration, often called diffusive shock acceleration (DSA), is believed to be the primary acceleration mechanism in most collisionless MHD shocks. This phenomenon arises when charged particles interact quasi-elastically with turbulent fields in the shock layer and are diffusively transported back and forth across the shock, each time achieving a net gain in energy on average. Monte Carlo simulations of this process (see Jones & Ellison 1991 and references therein) have had great success in modeling shocks inside the heliosphere and comparing them directly with in situ measurements from various spacecraft (e.g., Ellison et al. 1990b; Baring et al. 1997; Summerlin & Baring 2006). It is quite likely that this same process is responsible for the power-law tails inferred in astrophysical shocks, including relativistic MHD discontinuities such as those believed to be associated with blazars (e.g., see, Stecker et al. 2007) and GRBs (e.g., see reviews by Piran 1999; Mészáros 2001).

Early work on relativistic shocks was mostly analytic in the test-particle approximation (e.g., Peacock 1981; Kirk & Schneider 1987; Heavens & Drury 1988; Kirk & Heavens 1989), where the accelerated particles do not contribute significantly to the global MHD structure of the shock. Since such systems are inherently anisotropic, due to rapid convection of particles through and away downstream of the shock, the diffusion approximation cannot be applied. This renders analytic approaches, such as solution of the diffusion-convection Fokker–Planck equation, more difficult for ultrarelativistic upstream flows, though advances can be made in special cases, such as the limit of extremely small angle scattering (SAS; e.g., Kirk & Schneider 1987; Kirk et al. 2000). Accordingly, complementary Monte Carlo techniques, first developed for non-relativistic shock applications by Ellison et al. (1981), have been employed for relativistic shocks by a number of authors, including test-particle analyses for steady state shocks of parallel and oblique magnetic fields by Ellison et al. (1990a), Ostrowski (1991), Bednarz & Ostrowski (1998), Baring (1999), Niemiec & Ostrowski (2004), Ellison & Double (2004), and Stecker et al.

(2007). It is such a simulational approach that is highlighted here; its accessibility to broad dynamic ranges in momenta is extremely desirable, providing a niche for Monte Carlo techniques in connecting with observations of astronomical objects such as GRBs and blazars.

It should be noted that the most comprehensive way to study dissipation, acceleration, and wave generation in collisionless shocks is with particle-in-cell (PIC) simulations, where particle motion and field fluctuations are obtained as solutions of the Newton–Lorentz and Maxwell's equations. Relativistic PIC codes have blossomed to model shocks in applications such as GRBs and pulsar wind termination shocks, focusing largely, but not exclusively, on perpendicular shocks (e.g., Gallant et al. 1992; Smolsky & Usov 1996; Silva et al. 2003; Hededal et al. 2004; Liang & Nishimura 2004; Medvedev et al. 2005; Nishikawa et al. 2005; Spitkovsky 2008). These works have explored pair shocks, ion-doped shocks, Poynting flux-dominated outflows, and low-field systems with dissipation driven by the Weibel instability. PIC simulations are dynamic in nature, and rarely achieve a time-asymptotic state. None of these works has demonstrated the establishment of an extended power law that is required in modeling emission from GRBs and active galactic nuclei (AGNs), though note the isolated recent suggestion (Spitkovsky 2008; Sironi & Spitkovsky 2011) of a non-thermal tail generated by diffusive transport. The general difficulty with explicitly seeing acceleration in PIC codes beyond true thermalization is perhaps due to the severely restricted spatial and temporal scales of the simulations, imposed by their intensive CPU and memory requirements. With the anticipated advances in computational capability over the next decade, PIC simulations will become a much more powerful tool for probing DSA. For a discussion of relativistic shock acceleration, see Baring (2004).

To date, much simulational work on DSA at relativistic shocks has focused on parallel systems (where the magnetic field direction is parallel to the shock normal) in which particles experience frequent SASs, as opposed to infrequent large angle scatterings (LASs). In the limit of ultrarelativistic shock speeds, for differential particle distributions $dn/dp = p^{-\sigma}$, a power-law index of $\sigma \approx 2.23$ is realized, as can be found analytically (e.g., Kirk et al. 2000) and numerically (e.g., Bednarz & Ostrowski 1998; Baring 1999; Ellison & Double 2004). However, it is not necessary to assume that SAS is the dominant scattering mechanism, nor is it warranted in some situations: the phase space for the character of SAS to be realized shrinks with increasing shock Lorentz factor. Moreover, many astrophysical shocks, such as those in blazar jets, are either not parallel or not ultrarelativistic. Clearly, a more robust examination of the parameter space is desirable if one is to characterize the emission coming from these objects, and use it to probe their shocked plasma environments.

To achieve such a goal, here we have extended our Monte Carlo DSA code (Summerlin & Baring 2006) to include shocks of arbitrary speed and obliquity, including the trans-relativistic regime. Additionally, we generally presume an electron–positron plasma shock, following current thinking on the nature of GRB outflows (e.g., Piran 1999; Mészáros 2001) and blazar jets, though the results apply equally well to ion-dominated relativistic shocks. The global structure of the shocks is defined via the Rankine–Hugoniot relations, solved along the lines of previous expositions (e.g., Double et al. 2004). Principal output includes complete momentum and angular distributions, at different distances upstream and downstream of the shock. To demonstrate the validity of the simulation, and to distinguish its particular character, comparisons are made with both theoretical and simulation results of other papers (principally Kirk & Heavens 1989; Kirk et al. 2000; Ellison & Double 2004; Niemiec & Ostrowski 2004). More importantly, we expand on these previous works by exploring the parameter space for oblique relativistic shocks comprehensively, focusing on the shock obliquity, turbulence levels, and parameters encapsulating the microphysics of the turbulent interactions as key variables determining the high-energy power-law index of the particle distribution.

We find that, in relativistic shocks, unlike in non-relativistic shocks, the microphysics of the turbulence becomes an important factor in determining both the value of the power-law index and how many decades in energy particles are accelerated before a power law is achieved. Particles undergoing infrequent LASs consistently produce harder power laws than their SAS counterparts and take many more decades in energy to realize a smooth power law. It is also apparent that the power-law index is critically dependent upon the subluminality, versus superluminality, of the shock, as discussed in Section 4. We find that, as do Ellison & Double (2004) and Baring (2004), in superluminal shocks, the power law rapidly becomes softer with decreasing levels of turbulence and increasing obliquity, due to the difficulty particles have returning to the shock once they have crossed to the downstream side.

In distinct contrast, in the case of subluminal shocks, a decreased amount of turbulence and increased obliquity can actually render the acceleration process far more efficient as particles undergo the coherent process of shock drift acceleration (SDA), where some particles persistently gyrate in the shock layer, preferentially gaining energy due to the kinking of the magnetic field. In the limit of no cross-field diffusion and a de Hoffmann–Teller frame velocity of nearly c, explored theoretically by Kirk & Heavens (1989) using semianalytic solutions to the diffusion-convection equation, an extremely low value of the power-law index around $\sigma = 1$ becomes possible. However, with our simulation, we are able to more readily isolate how such flat distributions arise. In marginally subluminal shocks with SAS operating, a small fraction of high-energy particles are reflected off the shock by the kink in the magnetic field. For those that are reflected, the angular distribution for subsequent shock encounters is such that the transmission region is almost entirely depleted, resulting in virtually 100% reflection at each shock encounter. These particles essentially become trapped and are accelerated to very high energies very quickly, before they are eventually lost downstream. The extremely low levels of turbulence necessary to permit SDA to act unabated almost certainly do not occur in Nature, but the effects of SDA can be seen to a lesser degree in shocks with more realistic parameters. In general, it can be concluded that the power-law indices in relativistic shocks can sample a broad range, depending on the three basic system parameters explored here. After outlining our simulation technique in Section 2 and summarizing our method for determining the shock jump conditions in Section 3, our results are presented in Section 4, and then interpreted in the context of blazars in Section 5.

2. THE MONTE CARLO SIMULATION TECHNIQUE

The Monte Carlo Simulation technique employed in this paper closely follows the pioneering work on this method by Ellison et al. (1981) and Ellison & Eichler (1984); see

Jones & Ellison (1991) for a review. It is a test-particle simulation that models convection and diffusion of charges in a turbulent, shocked flow, complementing the analytic approach of Bell (1978) that was extended to the relativistic regime by Peacock (1981). It has been successfully applied in a variety of environments including Earth's bow shock (Ellison et al. 1990b), interplanetary shocks (e.g., Baring et al. 1997; Summerlin & Baring 2006), the solar wind termination shock (see Ellison et al. 1999), supernova remnants (see Baring et al. 1999; Baring & Summerlin 2007), and in the regime of highly relativistic shocks that is generally encountered in extragalactic contexts (e.g., Ellison et al. 1990a; Ellison & Double 2004; Stecker et al. 2007). The code models particle gyration about bulk magnetic fields in convecting fluid flows, while having their trajectories perturbed by embedded hydromagnetic turbulence. The perturbations mediate spatial diffusion that permits some small fraction of particles to transit the shock front multiple times, kinematically sampling the difference in flow speeds on either side of the shock, and thereby being accelerated via first-order Fermi (or diffusive) shock acceleration (see Bell 1978; Jones & Ellison 1991). The code is fully relativistic and transitions seamlessly from non-relativistic to relativistic flow regimes; it also treats arbitrary orientations of the mean magnetic field.

The simulation space is divided into a distinct number of grid zones distributed along the x-axis, which is here defined to be the direction normal to the planar shock surface. The boundaries of these grid zones are locations where the bulk properties of the fluid (flow speeds, magnetic fields, etc.) can change. The values of these fluid properties are specified a priori, and for the test-particle implementation of the simulation in this paper, have fixed values throughout the simulation runs. In the simulations presented in this paper a simple step function shock is used with only two grid zones: one upstream and one downstream. The field and fluid quantities in these two zones are related by the fully relativistic, Rankine–Hugoniot jump conditions, as discussed in Section 3 below. This construction facilitates the generalization to nonlinear acceleration regimes (e.g., Ellison & Eichler 1984; Ellison et al. 1996; see also Ellison & Double 2002 for the first treatment of nonlinear modification of relativistic shocks), where the energetic particles contribute to the grid-by-grid specification of MHD quantities constrained by energy/momentum flux conservation.

Particles are injected isotropically into the system anywhere along the x-axis, though usually an upstream injection is adopted. The energy distribution of injected particles can be either mono-energetic, a thermal Maxwell–Boltzmann form at any temperature (relativistic or non-relativistic), or a power-law distribution in momentum of arbitrary index. For non-relativistic shocks with thermal particle injection, the code automatically calculates the Rankine–Hugoniot shock jump conditions to ascertain the downstream fluid and field vector values. For relativistic shocks, the jump condition solution technique is necessarily more complicated, as described in Section 3. This solution is accomplished outside the simulation program, and the jump conditions are then input manually as initial conditions for the simulation runs. The code can also include multiple species of charged particles (e.g., treating hydrogenic and pair plasmas, and even contributions from helium) besides the test particles in the determination of the jump conditions. After particles are injected into the upstream fluid, they are allowed to gyrate in the local bulk magnetic field, convecting with the fluid, until it is determined that a phenomenological scattering occurs.

The effects of magnetic turbulence are simulated by specifying a local *fluid frame* mean free path for particle diffusion, given by

$$\lambda \;=\; \lambda_0 \left(\frac{r_g}{r_{g1}}\right)^{\alpha} \;\propto\; p^{\alpha}, \quad \lambda_0 = \eta r_{g1}, \tag{1}$$

where $r_g = pc/(qB)$ is the gyroradius of an ion or electron of momentum $p = mv$, mass m, and charge q in a magnetic field $B = |\mathbf{B}|$. Also $r_{g1} = mu_{1x}c/(qB)$ is the gyroradius of an ion with a speed v equal to the velocity component, u_{1x}, of the far upstream flow normal to the shock plane; here x denotes the direction normal to the shock. Without loss of generality, the mean free path scale λ_0 is set proportional to r_{g1} with constant of proportionality η defined via Equation (1). This phenomenological prescription for scattering was adopted in numerous papers outlining results from the Monte Carlo technique, including Ellison et al. (1981, 1990a, 1995, 1996) and Stecker et al. (2007). Following this and other previous Monte Carlo work, for simplicity, we set $\alpha = 1$, a specialization that is appropriate for traveling interplanetary shocks; see Ellison et al. (1990a, 1990b), Mason et al. (1983), and Giacalone et al. (1992) for discussions about the micro-physical expectations for α. The simulation can easily accommodate other values of α; however, the spectral results are somewhat insensitive to the choice of this parameter—its dominant effect is to modify the relative scale lengths for diffusion at different particle momenta. Since $\lambda \geqslant r_g$ is required for physically meaningful diffusion resulting from gyroresonant wave–particle interactions, the $\alpha = 1$ case is also motivated on fundamental grounds. The mean free path represents the spatial scale in the local fluid frame on which the momentum vector is deflected by $\pi/2$, on average. Note that for diffusion that is driven by non-gyroresonant interactions with field turbulence, perhaps grown via filamentation or Weibel instabilities, it is quite possible to sample $\eta < 1$ regimes, especially when the ambient magnetic field is quite low. Diffusion in this domain resembles the Bohm limit of $\eta = 1$ for gyroresonant diffusion, and accordingly the distributions for shock-accelerated charges are only mildly dependent on η when it is less than unity. For high Alfvénic Mach number shocks, the scattering is approximately elastic in the fluid frame, i.e., $|\mathbf{p}|$ is conserved in this frame for interactions with field turbulence that perturb a particle's pitch angle θ, gyrophase, and orbital gyrocenter.

When the Alfvénic Mach number $\mathcal{M}_A$ is low, the Alfvén waves move with appreciable speed in the fluid frame, so that partial inelasticity in scatterings arises. This yields second-order, stochastic diffusion contributions. While these can be routinely modeled in the simulation, inspection of Equations (8) and (10) of Pryadko & Petrosian's (1997) quasi-linear stochastic acceleration formalism clearly indicates that the stochastic contribution to the spatial diffusion coefficients is smaller than the first-order Fermi one by the order of $1/\mathcal{M}_A^2$. For the efficient generation of the high-energy power-law tails that are the primary focus of this paper, the astrophysical shocks of interest generally have large enough Alfvénic Mach numbers to neglect the effects of second-order acceleration. However, note that for near-luminal shocks at slightly suprathermal energies, particles are generally unable to convect upstream against the downstream flow and are inexorably swept downstream. In this energy regime, other mechanisms acting in the shock environs such as second-order Fermi acceleration or electrostatic cross-shock potentials may noticeably broaden/heat the downstream distribution function. This can then enhance injection into

the first-order acceleration process, and thereby affect the normalization of the power-law tail that results, particularly in cases of strongly inhibited injection. Treatment of stochastic acceleration effects will be deferred to future work.

The simplest invocation of scattering is to isotropize the fluid frame momentum over the surface of the sphere in momentum space (Ellison et al. 1990a). This is LAS, and physically corresponds to large magnetic disturbances that completely disrupt trajectories of particles. To model moderate or even smaller disturbances, each scattering event can be restricted to a much smaller solid angle, i.e., can be isotropic on a conical sector of a momentum sphere. The angular extent of this spherical sector $\delta\theta_{\rm max}$ becomes an additional parameter for the diffusion. Then multiple scattering events are required to realize a full mean free path. This is the scattering construct that is employed in this paper. The relationship between $\delta\theta_{\rm max}$ and λ was originally developed in Ellison et al. (1990a), but is more succinctly presented in Ellison & Double (2004) via

$$\delta\theta_{\rm max} = \sqrt{\frac{12\pi r_g}{\lambda N}}, \quad (2)$$

where r_g is the gyroradius and N is the number of times per gyroradius the particle is scattered. The limit of SAS corresponds to $N \gg 1$, for which the increment $\delta\mathbf{p}$ in momentum in a scattering satisfies $|\delta\mathbf{p}|/|\mathbf{p}| \sim \delta\theta_{\rm max}$. In practice, as will become evident below, for relativistic shocks the SAS domain is realized when the scattering angle satisfies $\delta\theta_{\rm max} \ll 1/\Gamma_1$, where $\Gamma_1 = 1/\sqrt{1 - u_{1x}^2/c^2}$ is the bulk Lorentz factor of the upstream fluid in the shock rest frame.

Cross-field diffusion emerges naturally from this scattering mechanism since, at every scattering, the particle's momentum vector is shifted in the local fluid frame, with the resulting effect that the gyrocenter of the particle is shifted randomly by a distance of order $r_g \sin\theta$ in the plane orthogonal to the local field. Transport perpendicular to the field is then governed by a kinetic theory description, so that the ratio of the spatial diffusion coefficients parallel ($\kappa_{||} = \lambda v/3$) and perpendicular ($\kappa_\perp$) to the magnetic field is given by $\kappa_\perp/\kappa_{||} = 1/(1+\eta^2)$ (see Forman et al. 1974; Ellison et al. 1995 for detailed expositions). Hence, η couples directly to the amount of cross-field diffusion and is a measure of the level of turbulence in the system, i.e., is an indicator of $\langle \delta B/B \rangle$. The quasi-isotropic diffusion case of $\eta = 1$ constitutes the Bohm diffusion limit, presumably corresponding to $\langle \delta B/B \rangle \approx 1$.

As will become clear in Sections 4.2 and 4.3, in oblique relativistic shocks, the resulting energy spectrum is critically dependent upon both η, due to the necessity of cross-field diffusion, and the scattering angle $\delta\theta_{\rm max}$, due to beaming effects, producing a broad range of power-law indices. For SAS regimes, $\delta\theta_{\rm max} < 1/\Gamma_1$, there is little variation in the power-law tails when other parameters are held constant, since the scatter angle is now less than the relativistic beaming angle, and the diffusion process becomes insensitive to the scattering kernel. Except for Section 4.4, SAS is deployed throughout this paper. Examples of the differences between SAS and LAS in relativistic shocks can be seen in Figure 2 of Stecker et al. (2007) and also in Figure 12.

In between each of the N scatterings per mean free path, the code calculates shock frame gyro-orbit trajectories using a semianalytic solver rather than the more popular Bulirsch–Stoer method (Stoer & Bulirsch 1980). Using the properties of the magnetized fluid, the shock frame position as a function of time is easily derived analytically. The particle is then moved along this analytic trajectory until one of two conditions is met: (a) the particle scatters or (b) the particle reaches the edge of a grid zone. The solution for the time it takes a particle to reach the edge of a grid zone must be performed numerically, since it involves roots of a transcendental equation of motion in the shock frame—the simulation employs a standard bisection technique for this purpose. When a particle crosses a grid zone boundary, the local fluid properties change, and the trajectory is recalculated and the propagation continues. When distances between scatterings are many gyro-radii, the semianalytic method can go from one scattering to the next in one step, covering many gyro-orbits in a single computational step. The Bulirsch–Stoer method will always require at least several steps per gyro-orbit due to the curvature of the trajectory. However, if particles scatter many times in one gyroradius, the increased overhead of the semianalytic method makes it slower than the Bulirsch–Stoer method, but not unreasonably so.

Particles that do not immediately return to the shock may isotropize in the downstream reference frame once they have traveled, on average, one mean free path. At this juncture, an analytical formula developed originally by Bell (1978) and later shown to be applicable to relativistic shocks by Peacock (1981; see also Jones & Ellison 1991) can be used to calculate the probability P_r that a particle heading downstream through a y–z plane at a particular distance x downstream will return upstream of this plane:

$$P_r = \left(\frac{v_f - u}{v_f + u}\right)^2. \quad (3)$$

In the above equation, u is the local downstream flow speed and v_f is the speed of the particle in this fluid frame. Particles that are deemed to fail to return are removed from the system. For those ascertained to be returning, their vector velocity components are also determined probabilistically. The particles are isotropic in the local fluid frame and have constant energy in the downstream frame of reference thanks to the elastic scattering off magnetic turbulence. So, the probability of a particle of a given fluid frame momentum returning with a particular angle cosine with respect to the shock normal, μ_s, can be found for arbitrary values of the particle speed and downstream flow speed. The details of this calculation and final result can be found in the Appendix, specifically Equation (A7). Employing this result, a simple accept–reject method (Garcia 2000, chap. 11) can be used to select a value for μ_s for particles determined to have returned. This statistical decision algorithm circumvents excessive computations of extensive downstream diffusion that are irrelevant to the acceleration process; accordingly, it speeds up the simulation dramatically. Using the correct angular distribution of returning particles, i.e., Equation (A7), is essential, guaranteeing that the complete distribution function of particles anywhere upstream of the probability of return plane is independent of the choice of x, provided $x > \lambda$, and isotropy in the fluid frame is satisfied at x.

For simulation output, accounting of particles in distinct momentum bins is documented. As a result of statistical losses in the downstream region, when less than half of the particles originally recorded in a given momentum bin are retained, the remaining particles are "split" into two particles each with half the "counting" value of the original. This technique of particle splitting allows the simulation to maintain good statistics over a large energy range. This extensive energy range is one of the primary advantages that the Monte Carlo technique has

over other types of simulations. Compared to hybrid plasma simulations and PIC simulations, Monte Carlo simulations are computationally inexpensive, allowing the simulation to be run long enough for particles to be accelerated to very high energies, well above that of the incoming upstream ballistic flow, in a reasonable amount of time.

In the test-particle implementation employed here, the characteristics of the shock and the functional form of the turbulence are specified a priori. The test-particle approximation is entirely appropriate unless there is a significant fraction of the total energy present in the accelerated particles. Since the distribution of these particles is only known after the simulation accelerates them, the shape of the shock cannot be adjusted to account for their existence until after the simulation is run. For non-relativistic shocks, Ellison & Eichler (1984) developed a feedback loop technique where subsequent runs calculate the modified hydrodynamic shock structure, based upon the accelerated particle distributions of the previous iterations; this nonlinear acceleration method is not employed here. Also, since the choice of the scattering mechanism can affect both injection and acceleration of particles, it can strongly impact nonlinear modifications for relativistic shocks. The influence of different scattering scenarios in such nonlinear acceleration systems will be the subject of future work.

This implementation also does not retain accounting of the amount of time the particle would have spent downstream of this "return" plane. In the event that acceleration time information is needed, a retrodictive approach described first in Jones (1978) and later applied directly to a Monte Carlo simulation in Ellison et al. (1990a) can be used. One important finding is that the interplay between energy boosting and time dilation effects leads only to modest changes (Baring 2002) in the acceleration time at plane-parallel relativistic shocks compared with standard non-relativistic shock formalism (Forman et al. 1974). The consideration of particle acceleration times is beyond the scope of the present work and will be deferred to a future investigation.

3. MAGNETOHYDRODYNAMIC JUMP CONDITIONS FOR OBLIQUE RELATIVISTIC SHOCKS

In the case of relativistic shocks, the shock jump conditions are considerably more difficult to solve than the non-relativistic solutions presented in Decker (1988) due to the impact of length contraction and time dilation effects on the structure of the six conservation equations. There are different approaches to solving the Rankine–Hugoniot jump conditions in relativistic MHD discontinuities, surveyed in Double et al. (2004; see also Gerbig & Schlickeiser 2011 for a recent exposition). Our approach here builds upon previous work by Ballard & Heavens (1991) that formulates the Rankine–Hugoniot conditions in the de Hoffmann–Teller frame (de Hoffmann & Teller 1950, hereafter HT) in a manageable form. The HT frame is a shock rest frame in which there are no $\mathbf{u} \times \mathbf{B}$ drift electric fields. This can be obtained from the local fluid frame by boosting along $\mathbf{B}$, but can also be obtained as a combination of two boosts along the axes of the coordinate system to avoid a rotation of the coordinate system. The system of equations is then transformed from the HT frame into the normal incidence frame (NIF, in which the upstream plasma flow is parallel to the shock normal or the $\hat{x}$-direction), arriving at a system of three comparatively simple simultaneous equations in which the terms that become imaginary in superluminal shocks are no longer present. These three equations are solved numerically after the Jüttner–Synge (J-S) equation of state (EOS) is invoked to connect key thermodynamic quantities, such as pressure and enthalpy, to the temperatures of the upstream and downstream relativistic Maxwell–Boltzmann distributions. This method encompasses a broad range of shock conditions, specifically ranges of sonic and Alfvénic Mach numbers, and transitions seamlessly from subluminal to superluminal regimes. Our results are compared directly with that of the work by Double et al. (2004), highlighting similarities, and also differences that result from a specific approximation to the downstream EOS employed in that work.

Before embarking upon the construction and reduction of the jump conditions, a brief summary of the subscript conventions adopted here for the different frames of reference is given. The "f" subscript will denote a quantity defined in the rest frame of the upstream (subscript 1) or downstream (subscript 2) plasma. HT frame variables will be subscripted with an "HT." To distinguish NIF frame quantities from those measured in the fluid or HT frames, they will be denoted by an "S" subscript for the shock frame. Additionally, $\Theta_{\rm B}$ will always refer to an angle the magnetic field $\vec{\boldsymbol{B}}$ makes with the shock normal, and $\theta_{\rm u}$ will refer to the angle a plasma flow makes with the shock normal. When the HT frame is found via a single boost along the direction of the magnetic field, the field components are identical in the local fluid and HT frames, often the "f" and "HT" subscripts will be explicitly omitted for compactness of notation, i.e., $B_1 \equiv B_{1\rm f} \equiv B_{1\rm HT}$, etc.

The character of the solutions to this system of equations is controlled by two key parameters, basically the relative scaling of the upstream thermal energy or pressure P_1, and the fluid frame magnetic field energy density $B_{1\rm f}^2/(8\pi)$ to the upstream ram pressure $\rho_1 u_{1x}^2$. Here, $u_{1x} = \beta_{1\rm xS} c$ is the velocity component of the upstream fluid normal to the shock, in the NIF. Accordingly, we define these via the sonic ($\mathcal{M}_{\rm S}$) and Alfvénic ($\mathcal{M}_{\rm A}$) Mach numbers:

$$\mathcal{M}_{\rm S}^2 = \frac{\rho_1 u_{1x}^2}{\gamma_{g1} P_1}, \quad \mathcal{M}_{\rm A}^2 = \frac{4\pi \rho_1 u_{1x}^2}{B_1^2}. \tag{4}$$

These are conventional definitions for non-relativistic shocks, and their extension to oblique discontinuities and relativistic systems does not lead to unique choices. For example, subjectivity is involved in deciding between u_{1x} and u_1, and similarly for $B_{1x\rm f}$ versus $B_{1\rm f}$. Hence, we adopt the above definitions (as did Double et al. 2004), for which γ_{g1} is the upstream adiabatic gas index, discussed further in Section 3.3, so that $\gamma_{g1} P_1/\rho_1$ is the square of the upstream sound speed.

3.1. The de Hoffmann–Teller Frame Solution

For subluminal flows, where $\beta_{1x}/\cos\Theta_{\rm Bf1} < 1$, the HT frame is an obvious choice in which the shock jump conditions can be written, since therein the jump conditions reduce to a simple form because the fluid flows along the magnetic field lines and there is no $\vec{\boldsymbol{u}} \times \vec{\boldsymbol{B}}$ electric field. For the time being, we will restrict considerations to these types of shocks and later trivially generalize the results to include superluminal shocks. Four of the shock jump equations are defined by the conservation of the mass, momentum (two components), and energy fluxes across the shock interface are conserved. The remaining two derive from the electromagnetic field constraints $\nabla \cdot \vec{\boldsymbol{B}} = 0$ and $\nabla \times \vec{\boldsymbol{E}} = \vec{\boldsymbol{0}}$, the latter of which is trivial in the HT frame, because $\vec{\boldsymbol{E}} = \vec{\boldsymbol{0}}$ identically everywhere.

The form of these jump conditions in the HT frame has been derived previously by Ballard & Heavens (1991). Those

equations are reproduced below with the notable exception that the subscript "y" used in their paper has been replaced with the subscript "z" to avoid confusion when comparing to other works. Here, the x-direction defines the normal to the shock plane in the HT frame, the magnetic field everywhere lies in the x–z plane, and the y-axis defines the direction of $\vec{\boldsymbol{u}} \times \vec{\boldsymbol{B}}$ drift velocities. All quantities save Γ, $\vec{\boldsymbol{\beta}}$, and $\vec{\boldsymbol{B}}$ are defined in the frame where the plasma is stationary hereafter referred to as the "local fluid frame" or "upstream/downstream rest frame." For the present, those three quantities are defined in the HT frame. Setting $c = 1$, as is done throughout this paper, conservation of mass or particle number flux along the shock normal gives

$$\Gamma_1 \beta_{1x}\, \rho_1 \;=\; \Gamma_2 \beta_{2x}\, \rho_2, \tag{5}$$

where ρ_i denotes mass density, and subscripts 1 and 2 denote upstream and downstream quantities (labeled by i in general). Throughout this subsection, HT subscripts will be omitted, but implied. Also, β is the flow speed written as a fraction of the speed of light, and $\Gamma = 1/\sqrt{1-\beta_x^2-\beta_z^2}$ is the Lorentz factor associated with the flow speed β. Conservation of the x- and z-components of momentum flux gives, respectively,

$$\begin{aligned} \Gamma_1^2\beta_{1x}^2\, w_1 + P_1 + \frac{B_{1z}^2}{8\pi} &= \Gamma_2^2\beta_{2x}^2\, w_2 + P_2 + \frac{B_{2z}^2}{8\pi} \\ \Gamma_1^2\beta_{1x}\beta_{1z}\, w_1 - \frac{B_{1x}B_{1z}}{4\pi} &= \Gamma_2^2\beta_{2x}\beta_{2z}\, w_2 - \frac{B_{2x}B_{2z}}{4\pi}. \end{aligned} \tag{6}$$

This corrects an obvious typographical error in Equation (26) of Ballard & Heavens (1991) in their terms involving the enthalpies $w_i = e_i + P_i$. The internal energy e_i, which includes the rest mass energy density, can be related to P_i and ρ_i through an EOS, as is addressed in Section 3.3 below. In the HT frame, conservation of energy flux is simply

$$\Gamma_1^2 \beta_{1x}\, w_1 \;=\; \Gamma_2^2 \beta_{2x}\, w_2. \tag{7}$$

Here, the magnetic field contributions to the stress-energy tensor (see, for example, Equation (21) of Double et al. 2004) cancel to zero precisely because of the pair of equations

$$\frac{\beta_{1z}}{\beta_{1x}} \;=\; \frac{B_{1z}}{B_{1x}} \;\equiv\; \tan\Theta_{\rm BHT1}, \quad \frac{\beta_{2z}}{\beta_{2x}} \;=\; \frac{B_{2z}}{B_{2x}} \;\equiv\; \tan\Theta_{\rm BHT2}, \tag{8}$$

that defines the specific choice of the HT frame. The absence of such magnetic terms in the energy flux, combined with the compact nature of the momentum flux conditions, underlines the attractive simplicity of adopting the HT frame (compare, for example, with the electromagnetic stress tensor contributions to the momentum fluxes in Equations (25) and (26) of Double et al. 2004). The trivial $\nabla\times\vec{\boldsymbol{E}} = \vec{\boldsymbol{0}}$ can be eliminated, effectively being replaced by the HT frame definitions in Equation (8). Finally, the Maxwell equation $\nabla\cdot\vec{\boldsymbol{B}} = \vec{\boldsymbol{0}}$ defining the absence of magnetic monopoles gives

$$B_{1x} \;=\; B_{2x}, \tag{9}$$

unaltered by relativistic generalization because it is intrinsically relativistic.

Following Ballard and Heavens, Equations (8) and (9) can be used to eliminate the z-components B_{1z} and B_{2z}, and the downstream x-component B_{2x}. Their solutions were defined in terms of two upstream parameters $A = \Gamma_1 w_1/\rho_1$ and $C = B_{1x}^2/[4\pi\rho_1\gamma_{g1}\beta_{1x}]$. Here, as an alternative listing, we observe that the ratio C/A appears repeatedly in the resulting subset of processed equations, so we define this ratio via

$$\psi \;=\; \frac{B_{1x}^2}{4\pi\Gamma_1^2\beta_{1x}\, w_1} \;\equiv\; \frac{\cos^2\Theta_{\rm BHT1}}{\mathcal{M}_{\rm A}^2}\,\frac{\beta_{1x}\rho_1}{\Gamma_1^2 w_1}, \tag{10}$$

which, as a relativistically modified ratio of magnetic to thermal (plus rest mass) energy density, is essentially an adaptation of the inverse of the upstream plasma *beta parameter* $\beta_{\rm P} = 8\pi\, P_1/B_1^2$ to oblique, relativistic MHD flows. The second prescription for ψ uses the Alfvénic Mach number definition in Equation (4), together with identity of *total* magnetic fields in the fluid and HT frames, i.e., $B_{1\rm HT} = B_{1\rm f}$. The energy flux equation is most easily manipulated, dividing Equation (7) by the mass conservation in Equation (5):

$$\frac{\Gamma_1 w_1}{\rho_1} \;=\; \frac{\Gamma_2 w_2}{\rho_2} \;\equiv\; \frac{w_2}{\rho_2\sqrt{1-\beta_{2x}^2-\beta_{2z}^2}}. \tag{11}$$

This is just the constant A employed by Ballard & Heavens (1991). Next, dividing the z-component of momentum conservation in Equation (6) by Equation (7) solves for β_{2z}:

$$\beta_{2z} \;=\; \beta_{2x}\,\frac{\beta_{1z}}{\beta_{1x}}\left(\frac{\beta_{1x}-\psi}{\beta_{2x}-\psi}\right). \tag{12}$$

This can be inserted into Equation (11), eliminating β_{2z}. Observe that viable jump conditions are only realizable when $\psi < \beta_{2x}$. This is equivalent to requiring that the total Mach number be greater than unity. Finally, the x-component of momentum conservation in Equation (6) can be divided by Equation (7), producing

$$\begin{aligned} &\beta_{1x} + \frac{P_1}{\Gamma_1^2\beta_{1x}w_1} + \frac{\psi}{2}\left(\frac{\beta_{1z}}{\beta_{1x}}\right)^2 \\ &\quad = \beta_{2x} + \frac{P_2}{\Gamma_1^2\beta_{1x}w_1} + \frac{\psi}{2}\left(\frac{\beta_{1z}}{\beta_{1x}}\right)^2\left(\frac{\beta_{1x}-\psi}{\beta_{2x}-\psi}\right)^2. \end{aligned} \tag{13}$$

Here, expressing the ratio $\beta_{1z}/\beta_{1x} = \tan\Theta_{\rm BHT1}$ in terms of the de Hoffmann–Teller field angle $\Theta_{\rm BHT1}$, a constant for the shock structure, yields an alternative algebraic form. Observe also that the second term on the right-hand side is proportional to P_2/w_2 multiplied by w_2/w_1; the second factor can be expressed using Equation (11), and the first is a function of the downstream temperature T_2 through the EOS, to be defined in Section 3.3.

Equation (11), with Equation (12) inserted, and Equation (13) constitute a system of two simultaneous equations with unknowns P_2, w_2, and β_{2x}. However, w_2 will be related in Section 3.3 to P_2 via an EOS, rendering the system numerically solvable. This set of equations is simple and elegant, being virtually as compact as the system for jump conditions at relativistic, plane-parallel, hydrodynamic shocks (e.g., Blandford & McKee 1976). However, their validity is technically restricted to subluminal regimes where the HT frame formally exists. Therefore, to realize broader applicability, it is necessary to transform them to the normal incidence shock rest frame, and thereafter explore their numerical solution.

3.2. Transforming to the Normal Incidence Shock Frame

In subluminal cases where the HT frame exists, one can define a boost velocity β_t in the $\hat{z}$-direction that transforms from the NIF into the HT frame. The two key input quantities in this regard are $\beta_{1\rm xS}$, the shock speed in the upstream fluid frame, and

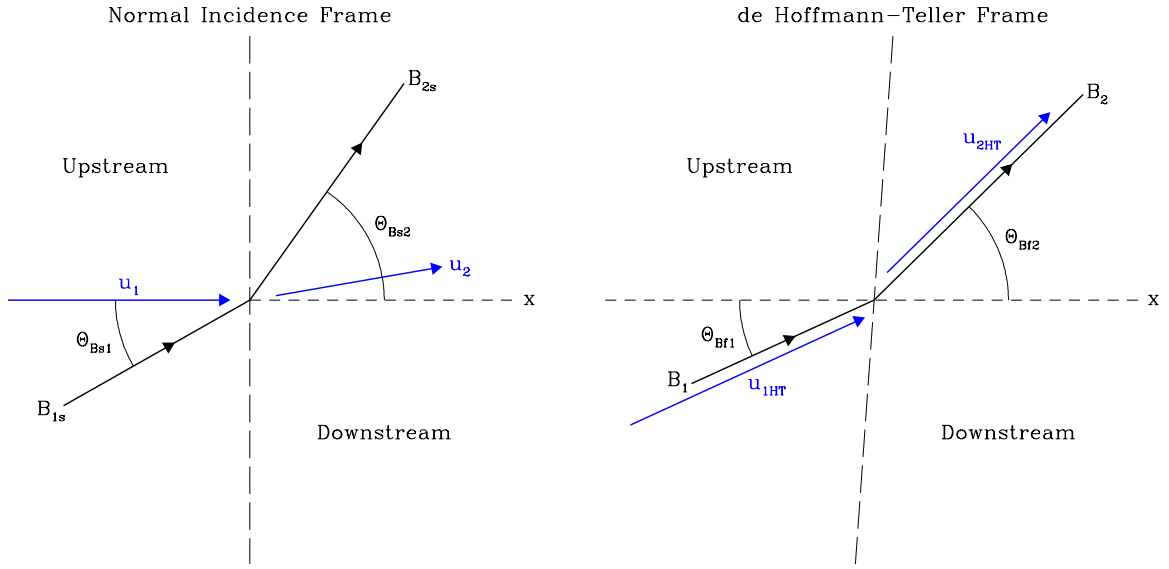

Figure 1. Geometry in the normal incidence (NIF; left panel) and de Hoffmann–Teller (HT; right panel) shock rest frames. Upstream flow speeds in the two reference frames are related by $u_{1\rm HT} \equiv \beta_{1\rm HT}c = u_1/\cos\Theta_{\rm Bf1}$. Upstream and downstream quantities are denoted by subscripts 1 and 2, respectively. In general, the NIF field angle $\Theta_{\rm Bs1}$ differs from the fluid frame/HT frame value $\Theta_{\rm Bf1} \equiv \Theta_{\rm BHT1}$, and likewise for the downstream angles. Also, in cases where the HT frame is obtained by boosting along the field fluid frame direction, the shock plane in the HT frame is rotated from that in the NIF due to relativistic aberration effects. For the two-step fluid-to-HT frame transformation protocol adopted here, the shock planes in the NIF and HT frames are coincident, i.e., no rotation is involved.

(A color version of this figure is available in the online journal.)

$\Theta_{\rm Bf1}$, the angle between the shock velocity and the magnetic field vector in the upstream fluid frame. A third parameter that is a derivative of these two is the HT frame field angle $\Theta_{\rm BHT1}$. As discussed by Kirk & Heavens (1989), there is a lack of uniqueness in defining field and flow angles in the de Hoffmann–Teller frame, up to rotations. Here, we will adopt the following sequence of boosts to effect Lorentz transformation to the HT frame from the local fluid frame: this will be performed by first boosting by $\beta_{\rm xS}\hat{x}$ along the shock normal to the NIF, and then boosting by $\beta_t\hat{z}$ in the shock plane to arrive at the HT frame. The planes of the shock in both the NIF and HT frames are thereby coincident. This yields a convenient definition of $\Theta_{\rm BHT1}$ (and $\Theta_{\rm BHT2}$) and is the preferred protocol for our simulation due to the enhanced simplicity it permits for modeling particle convection and gyration in the shock layer. However, it should be emphasized that a single boost along the field vector $\vec{\boldsymbol{B}}$ from the fluid-to-HT frames yields an aberration of the shock plane: it is rotated relative to the NIF shock plane, as described in Ballard & Heavens (1991), and is illustrated in Figure 1. Such a rotation leads to a need to account for it when defining field and flow angles with respect to the shock plane, an unnecessary complication. The two-step fluid-to-HT frame transformation approach adopted here was also the preference of Kirk & Heavens (1989).

The flow velocities in the NIF and HT frames of reference are related via standard Lorentz transformations

$$\beta_{\rm xHT} = \frac{\beta_{\rm xS}}{\Gamma_t(1+\beta_t\beta_{\rm zS})},$$
$$\beta_{\rm zHT} = \frac{\beta_{\rm zS}+\beta_t}{(1+\beta_t\beta_{\rm zS})}. \quad (14)$$

These relations can be applied to both the upstream and downstream sides of the shock; their subscripts 1, 2 have been suppressed here for the sake of compactness. In the upstream region, where the definition of the NIF requires that $\beta_{\rm zS} = 0$, these equations distill down to $\beta_{\rm xHT} = \beta_{\rm xS}/\Gamma_t$ and $\beta_{\rm zHT} = \beta_t$, respectively. Subsequently, taking the ratio of these two upstream equations, one can express the boost speed β_t and Lorentz factor $\Gamma_t = (1-\beta_t^2)^{-1/2}$ in terms of $\beta_{1\rm xS}$ and $\Theta_{\rm BHT1}$:

$$\Gamma_t\beta_t = \beta_{1\rm xS}\tan\Theta_{\rm BHT1},$$
$$\beta_t = \frac{\beta_{1\rm xS}\tan\Theta_{\rm BHT1}}{\sqrt{1+\beta_{1\rm xS}^2\tan^2\Theta_{\rm BHT1}}}. \quad (15)$$

Since, for flux conserving jump conditions in MHD discontinuities, the HT frame is identical for both upstream and downstream locations, it can be inferred that the identities in Equation (15) can also be written in terms of downstream quantities, merely via the substitutions $\beta_{1\rm xS} \rightarrow \beta_{2\rm xS}$ and $\Theta_{\rm BHT1} \rightarrow \Theta_{\rm BHT2}$.

The relationship between the magnetic field components in the two frames of reference is similarly routinely derived via standard transformation equations for electromagnetic fields:

$$B_{\rm xHT} = \frac{B_{\rm xS}}{\Gamma_t}, \quad B_{\rm zHT} = B_{\rm zS}, \quad (16)$$

noting that the equation for $B_{\rm xHT}$ is only one part of the full transformation equations, which also transform the NIF drift electric field in the $\hat{y}$-direction exactly to zero in the HT frame. The ratios of the equations in Equation (16) then simply yield

$$\tan\Theta_{\rm BHT1} = \Gamma_t\tan\Theta_{\rm Bs1}, \quad \tan\Theta_{\rm BHT2} = \Gamma_t\tan\Theta_{\rm Bs2} \quad (17)$$

for the upstream and downstream HT frame field angles to the shock normal. These are recognizable as aberration formulae for the electromagnetic/photon field, with the NIF frame field obliquity always being less than that in the de Hoffmann–Teller frame. Combining this result with Equation (15) yields the relationship

$$\beta_t = \beta_{1\rm xS}\tan\Theta_{\rm Bs1}, \quad (18)$$

removing a reference to the HT frame from Equation (14). The subluminal condition for the existence of the HT frame, written in terms of NIF quantities, is then $\beta_{1\rm xS}\tan\Theta_{\rm Bs1} < 1$.

To close this sequence of boost algebra, one needs the relation between field angles in the fluid frames and the NIF. These are derived in the same manner as Equation (17), yielding

$$\tan\Theta_{\rm Bs1} \;=\; \Gamma_{1\rm S}\tan\Theta_{\rm Bf1}\,, \quad \tan\Theta_{\rm Bs2} \;=\; \Gamma_{2\rm S}\tan\Theta_{\rm Bf2}\,, \tag{19}$$

where $\Gamma_{1\rm S} = 1/\sqrt{1-\beta_{1\rm xS}^2}$ and $\Gamma_{2\rm S} = 1/\sqrt{1-\beta_{2\rm xS}^2-\beta_{2\rm zS}^2}$. As a result, Equation (18) can be rewritten using $\tan\Theta_{\rm BHT1} = \Gamma_{1\rm S}\Gamma_t\tan\Theta_{\rm Bf1}$ to yield a boost speed expressed entirely in terms of input quantities:

$$\beta_t \;=\; \Gamma_{1\rm S}\beta_{1\rm xS}\,\tan\Theta_{\rm Bf1}\,. \tag{20}$$

This then routinely rearranges so that the subluminal $\beta_t < 1$ condition becomes the familiar $\beta_{1\rm xS}/\cos\Theta_{\rm Bf1} < 1$.

By replacing the HT frame quantities in Equations (11), (12), and (13) with their shock frame equivalents via Equations (14), (17), and (18), the Rankine–Hugoniot relations then become a system of three equations with unknowns P_2, w_2, $\beta_{2\rm xS}$, and $\beta_{2\rm zS}$ that possesses a non-singular mathematical character in the NIF frame at the luminal interface $\beta_{1\rm xS}/\cos\Theta_{\rm Bf1} = 1$. The system now retains only information about upstream and downstream fluid frame field angles and thermodynamic quantities, and the transformation velocities required to get to the NIF frame from the fluid frames. It must be emphasized that an attractive characteristic of this methodology is that significant cancellations remove any terms that become imaginary or unphysical in a superluminal shock, revealing a smooth mathematical transition of solutions from subluminal to superluminal regimes. The specification of an EOS that relates P_2 to w_2 closes this system, rendering it amenable to numerical solution.

3.3. The Equation of State

Assuming there are no shear stresses and axial symmetry about the magnetic field, the pressure tensor is diagonal. One can then form an isotropic pressure $P = (P_\parallel + 2P_\perp)/3$, where $P_\parallel$ and $P_\perp$ denote the pressure components, respectively, parallel to and perpendicular to the mean magnetic field. Then the "adiabatic" gas index γ_g, the approximate ratio of specific heats, can parameterize the EOS via the adiabatic expansion law for an ideal gas:

$$PV^{\gamma_g} \;=\; \text{constant}. \tag{21}$$

Here, γ_g ranges between $5/3$ for a non-relativistic, compressible gas, and $4/3$ for an ultrarelativistic gas. With the specification of this index, the internal (thermal) energy density $P/(\gamma_g - 1)$ is related to the pressure, so that the total internal energy density plus the rest mass energy density can be written as

$$e \;=\; \frac{P}{\gamma_g - 1} + \rho\,, \tag{22}$$

where, again, $c = 1$ has been assumed, as will be done throughout the rest of this work. Reintroducing the subscripts $i = 1, 2$ to label upstream and downstream fluid frames, this leads to the forms for the enthalpies that are deployed in the Rankine–Hugoniot relations:

$$w_i \;=\; e_i + P_i \;=\; \frac{\gamma_{gi}\,P_i}{\gamma_{gi} - 1} + \rho_i\,. \tag{23}$$

The particular values of γ_{gi} can be expressed as a moment of the fluid frame particle momentum distributions upstream and downstream, and so can apply to both thermal and non-thermal populations. While they are simply prescribed in the non-relativistic and ultrarelativistic asymptotic cases, a more precise formulation is required to treat the mildly relativistic domain.

Here, it is assumed that the background plasma possesses a relativistic thermal Maxwell–Boltzmann distribution that defines the J-S EOS (e.g., Synge 1957). Then, the temperature T can be the sole thermodynamic parameter, and all other thermodynamic quantities can be prescribed in terms of it. The EOS depends on the number of species, their masses, and the state of thermal equilibrium between the various species, i.e., the temperature equilibration or otherwise. For simplicity, a single component plasma is adopted here, appropriate for an electron–positron pair plasma as might be encountered in relativistic jets in extragalactic sources such as GRBs or blazars. Equations of states for electron–ion and other mixed species gases are addressed in Ballard & Heavens (1991). For a pair plasma, the enthalpy can be written in terms of modified Bessel functions:

$$\frac{w_i}{\rho_i} = R(\tau_i) + \tau_i\,, \quad R(\tau) = 3\tau + \frac{K_1(1/\tau)}{K_2(1/\tau)}, \tag{24}$$

where the K_i are modified Bessel functions of the second kind (e.g., see, pp. 708–715 of Arfken & Weber 2001) and

$$\tau_i \;=\; \frac{kT_i}{m_e} \;=\; \frac{P_i}{\rho_i}\,, \quad i = 1, 2, \tag{25}$$

is the dimensionless pair temperature (in units of $c = 1$). This EOS can treat arbitrary sonic Mach numbers, in distinct contrast to the approximation employed by Double et al. (2004), discussed below, that uses kinematics in high $\mathcal{M}_{\rm S}$ shocks to specify the downstream pressure.

A modest disadvantage of the J-S EOS lies in the complexity of the Bessel function; it is not conducive to either analytical or numerical solutions of Equations (11)–(13). However, noting the asymptotic behavior of Equation (24), namely, $R(\tau) \to 3\tau$ as $\tau \to \infty$, and $R(\tau) \to 1 + 3\tau/2$ as $\tau \to 0$, a remarkably good approximation for the function $R(\tau)$ is given by a Padé approximation of third order:

$$R(\tau) \;\approx\; \frac{2 + 7\tau + 12\tau^2 + 6\tau^3}{2 + 4\tau + 2\tau^2}. \tag{26}$$

This approximation is accurate to 0.25% over the entire domain and is slightly less algebraically complicated than the approximation in Equation (38) of Double et al. (2004). By inverting Equation (23) to obtain γ_{gi}, and using Equations (24) and (26), one can find γ_{gi} as a function of τ_i:

$$\gamma_{gi} \;=\; 1 + \frac{\tau_i}{R(\tau_i) - 1} \;\approx\; \frac{5 + 14\tau_i + 8\tau_i^2}{3 + 10\tau_i + 6\tau_i^2}. \tag{27}$$

Inserting the approximation from Equation (26) in Equation (24) provides w_i/ρ_i as a function of only τ_i, eliminating the fourth unknown quantity in Equations (11)–(13); this is the protocol adopted for the numerical solution of the Rankine–Hugoniot relations.

3.4. Numerical Solutions for the Jump Conditions

The resulting three equations were solved numerically using Mathematica. For the case of a plane-parallel shock, we compared directly with solutions displayed in Figure 1(b) of Heavens & Drury (1988) where downstream flow speeds are

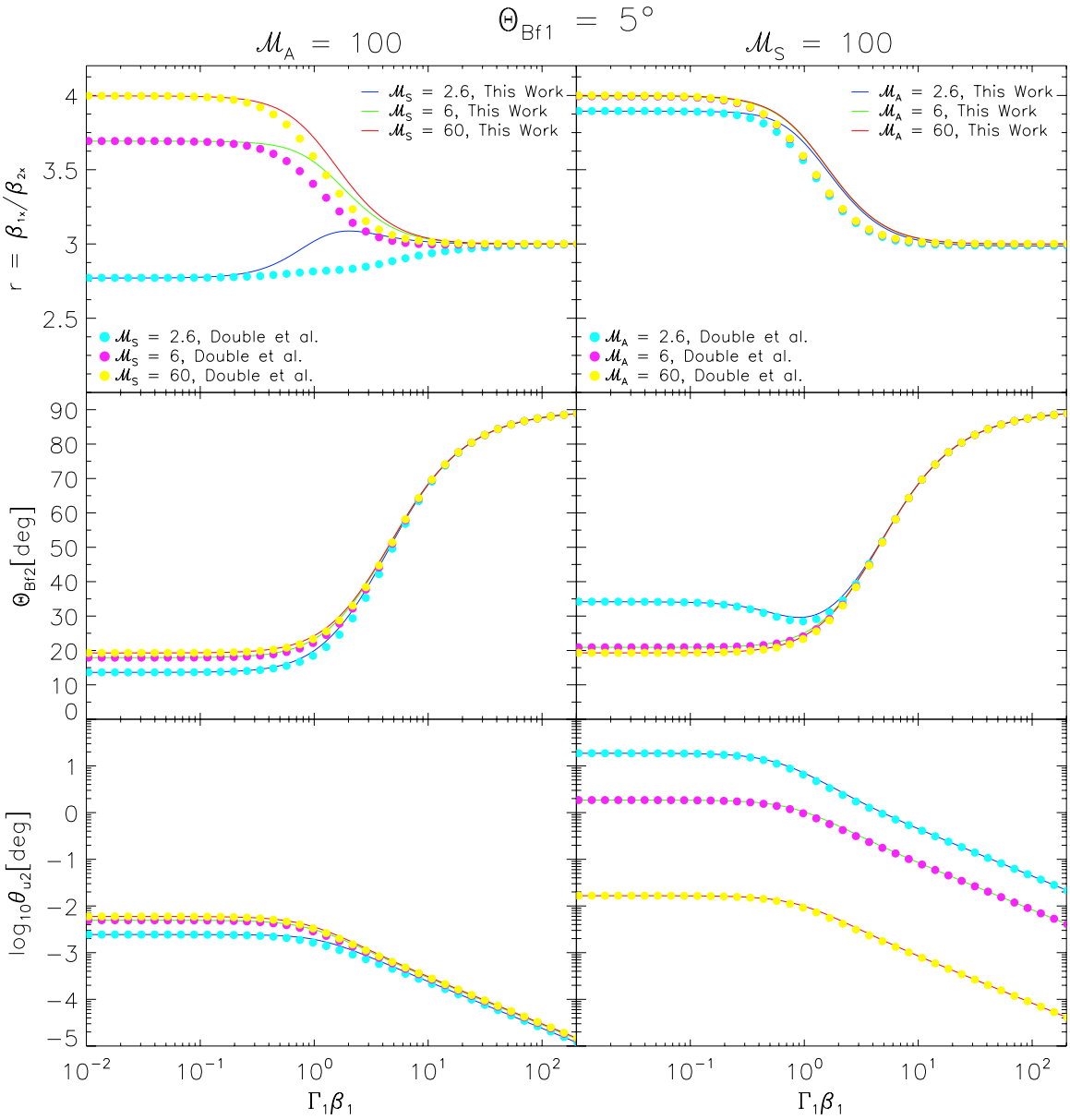

Figure 2. Rankine–Hugoniot relations for r, the compression ratio, Θ_{Bf2}, the angle the downstream fluid frame magnetic field makes with the shock normal, and θ_{u2}, the angle the downstream flow makes with the shock normal, as functions of the upstream NIF rapidity of the shock, $\Gamma_1\beta_1 \equiv \Gamma_{1S}\beta_{1xS}$. Solutions are displayed for various values of the Alfvénic ($\mathcal{M}_A$) and sonic ($\mathcal{M}_S$) Mach numbers, with the angle the upstream magnetic field makes with the shock normal, Θ_{Bf1}, set to 5°. Solid lines are new results from this work using the Jüttner–Synge (J-S) equation of state and Padé approximation described by Equation (26). Dotted curves represent results from the previous work of Double et al. (2004).

(A color version of this figure is available in the online journal.)

found as a function of upstream flow speeds for parallel ($\Theta_{Bf1} = 0°$) electron–positron shocks at various temperatures using the J-S EOS just as we do. We find no observable differences between our results and theirs for plane-parallel shocks. For the case of oblique shocks, representative solutions, as functions of the upstream fluid rapidity $\Gamma_1\beta_1 \equiv \Gamma_{1S}\beta_{1xS}$, are displayed in Figure 2 (quasi-parallel case) and Figure 3 (quasi-perpendicular shock). The plots exhibit the velocity compression ratio $r = \beta_{1xS}/\beta_{2xS}$, and the downstream fluid frame field and fluid NIF velocity angles to the shock normal. Observe that hereafter, the subscript "S" will be omitted when referring to NIF values for β_i and Γ_i. For the sake of comparison, these figures also display equivalent plots for the same sonic and Alfvénic Mach numbers (as defined in Equation (4)) and shock obliquities, taken from Double et al. (2004). It is evident that the solutions here closely match those of Double et al. in both the non-relativistic and ultrarelativistic regimes. The jump conditions reveal several characteristics, such as the declining compression ratio with declining Mach numbers of either variety, and small fluid deflections at the shock in the ultrarelativistic regime. There are noticeable differences between our solutions and those of Double et al. (2004) in the trans-relativistic domain, but mainly for just the compression ratio.

These differences in the two works, especially apparent for low sonic Mach numbers, are the result of two different assumptions regarding the EOS both upstream and downstream of the shock. In this work, the effective γ_{g1} for a given flow speed and Mach number can be determined using Equations (27) and (4). For $\mathcal{M}_S = 100, 60$, and 6, the upstream values of γ_{g1} stay within 1% of the nominal non-relativistic value of

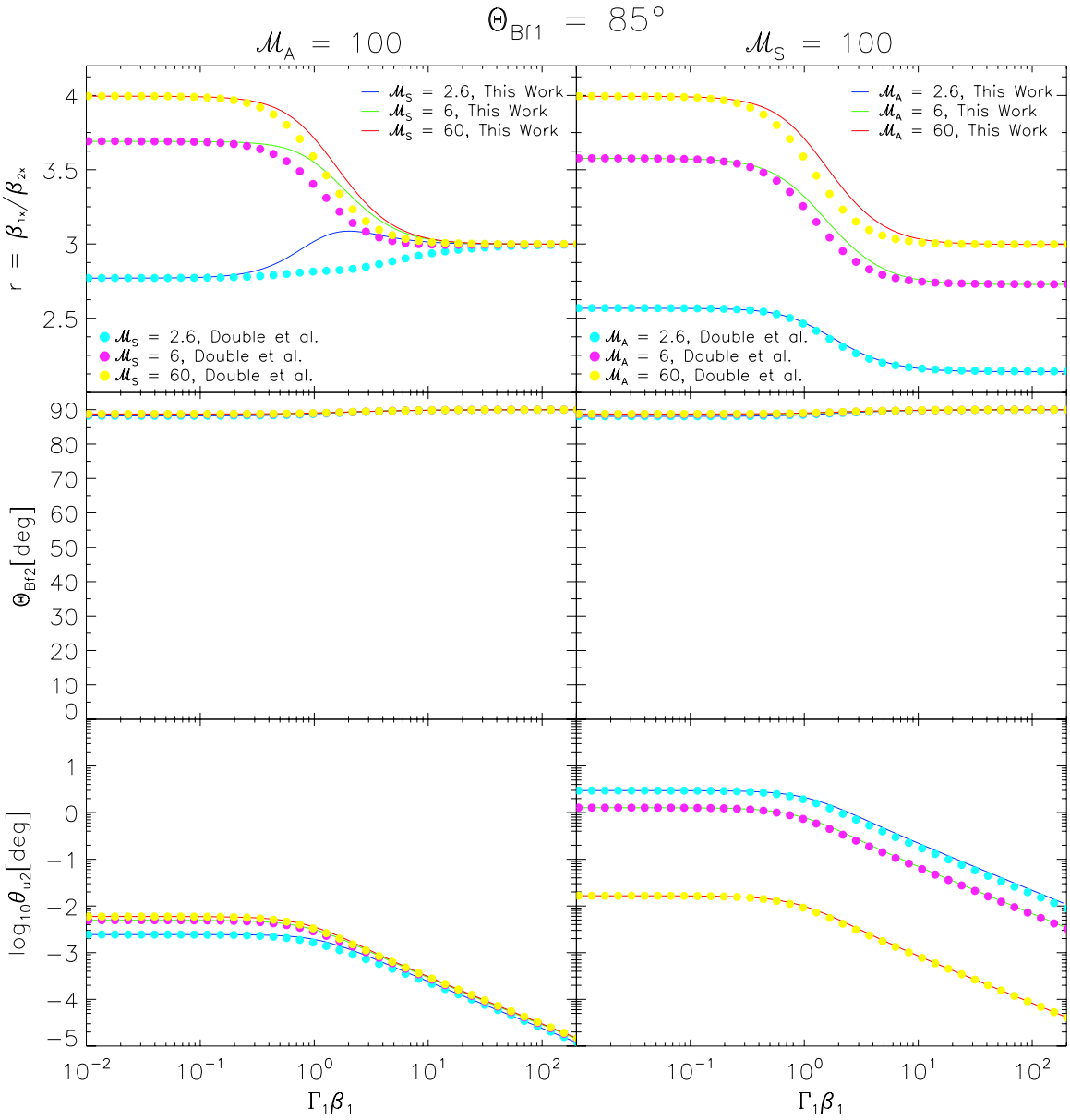

Figure 3. Solutions to the Rankine–Hugoniot relations for r, Θ_{Bf2}, and θ_{u2}, as in Figure 2. However, here, the upstream field obliquity is $\Theta_{Bf1} = 85°$, constituting quasi-perpendicular shocks. Values of the Alfvénic ($\mathcal{M}_A$) and sonic ($\mathcal{M}_S$) Mach numbers are as labeled. Again, solid lines are new results from this work using the Jüttner-Synge equation of state, while the dotted curves represent the solutions of Double et al. (2004).

(A color version of this figure is available in the online journal.)

5/3. However, in the $\mathcal{M}_S = 2.6$ case, we find $\gamma_{g1} \approx 1.6$ for large values of $\Gamma_1\beta_1$. In their work, Double et al. (2004) make an approximation assuming a cold upstream flow (i.e., a large sonic Mach number with upstream $\gamma_{g1} = 5/3$), resulting in the following equation relating the downstream γ_{g2} to the downstream flow speed rather than to the downstream pressure:

$$\gamma_{g2} = \frac{\Gamma_{rel}\beta_{rel}^2}{3(\Gamma_{rel}-1)} + 1 \equiv \frac{1+4\Gamma_{rel}}{3\Gamma_{rel}}, \quad (28)$$

where

$$\beta_{rel} = \frac{\beta_1 - \beta_2}{1-\beta_1\beta_2}, \quad \Gamma_{rel} \simeq \left(1-\beta_{rel}^2\right)^{-1/2}. \quad (29)$$

Note that the slight angle between the upstream and downstream NIF flow velocity vectors spawns the approximation for Γ_{rel}; the details and justification of this approximation can be found in Section 3.1 of their paper. Assuming that $\gamma_{g1} = 5/3$ then results in a small ~4% discrepancy in γ_{g2} relative to results from our J-S EOS, in the lowest Mach number cases. From the plots, clearly the numerical evaluations of the compression ratio are sensitive to the choice of the form of the downstream EOS, i.e., γ_{g2}.

In the limit that $\Gamma_1\beta_1$ approaches infinity, the details of the EOS become irrelevant, and a simple analytic solution can be found to approximate the results of both approaches. Defining

$$q = \frac{\mathcal{M}_A^2}{\sin^2\Theta_{Bf1}}\frac{w_1}{\rho_1} = \left(\frac{\mathcal{M}_S^2(\gamma_{g1}-1)+1}{\mathcal{M}_S^2(\gamma_{g1}-1)}\right)\frac{\mathcal{M}_A^2}{\sin^2\Theta_{Bf1}}, \quad (30)$$

one can write the asymptotic limit for the compression ratio as

$$r \approx \sqrt{4+4q+\frac{q^2}{4}} - 1 - \frac{q}{2}, \quad \Gamma_1 \gg 1, \quad (31)$$

which corresponds to Equation (47) of Double et al. (2004). The downstream fluid deflection and magnetic fields angles possess corresponding asymptotic forms for $\Gamma_1 \gg 1$ of

$$\tan\Theta_{\rm Bf2} \approx \Gamma_1 \tan\Theta_{\rm Bf1}\sqrt{r^2-1}, \qquad \tan\theta_{\rm u2S} \approx \frac{3-r}{2\Gamma_1\tan\Theta_{\rm Bf1}}. \tag{32}$$

When combined with Equation (9), the asymptotic equation for $\tan\Theta_{\rm Bf2}$ becomes Equation (40) of Double et al. (2004). Clearly, fluid deflection is very small for ultrarelativistic flows, the hallmark of the extreme inertia of the upstream fluid. One can see that, for the range of sonic Mach numbers explored here, the critical parameter q is a comparatively weak function of the sonic Mach number inducing less than a 50% change in q as the sonic Mach number varies from 2.6 to 60. In these cases, the Alfvénic Mach number and the upstream magnetic field angle $\Theta_{\rm Bf1}$ are more important for determining the asymptotic behavior of the jump conditions. It is also evident that since $r \approx 3$ when $\Gamma_1 \gg 1$ and $q \gg 1$, the downstream fluid deflection angle $\theta_{\rm u2S}$ in the shock frame is extremely small.

4. RESULTS

The simulation we have developed is capable of handling both subluminal and superluminal shocks of arbitrary obliquity. It can also simulate the effects of SAS or LAS with varying levels of cross-field diffusion controlled through the η parameter. These broad capabilities encapsulate a range of properties that are relevant to astrophysical shock environs such as those in extragalactic jets in GRBs and blazars. Moreover, they allow us to examine and expand upon a variety of previous investigations, including the semianalytic studies of Kirk et al. (2000) and Kirk & Heavens (1989) as well as other simulations, such as Ellison & Double (2004) and Niemiec & Ostrowski (2004). The following subsections highlight our key results in distinct parameter regimes: parallel shocks, oblique subluminal shocks, oblique superluminal shocks, and finally, LAS scenarios. Each of these sections provide physical scenarios where the power-law index is substantially different from the "canonical" $\sigma = -2.23$ (where $dn/dp = p^{-\sigma}$) result, which we demonstrate only holds at the shock location in parallel, ultrarelativistic ($\Gamma_1 \gg 1$) shocks with an SAS scenario, concurring with previous work. Altering this specific scenario yields power-law indices that depend on the microphysics (LAS versus SAS), shock obliquity ($\Theta_{\rm Bf1}$), and turbulence parameter (η) as well as the location relative to the shock front. A brief interpretation of these results in the context of blazars is offered in Section 5.

4.1. Parallel Shocks

Parallel shocks possess the important simplification that cross-field diffusion is immaterial. Accordingly, the model parameter η does not impact the spectra at the shock and serves only to define the diffusive scale along the shock normal. For the case of relativistic parallel shocks, the canonical result $\sigma = 2.23$ power-law spectrum was highlighted in the semianalytic study of Kirk et al. (2000), but had been found previously by Monte Carlo simulations (Bednarz & Ostrowski 1998; Baring 1999) and confirmed also by Ellison & Double (2004). However, exhibited results from these studies were spatially restricted to the immediate vicinity of the shock. The simulation presented here provides the opportunity to expand upon these studies and explore the spatial evolution of the particle distribution as well. The semianalytical work of Kirk et al. (2000) provides the best basis for benchmarking simulated distributions at the shock discontinuity. Accordingly, in this study, shock parameters are chosen in order to facilitate this comparison. The eigenfunction method of Kirk et al. (2000) built upon the earlier seminal work of Kirk & Schneider (1987) as an approach to solving the diffusion-convection equation in the neighborhood of a relativistic shock. Kirk et al. used this technique to generate power-law indexes and angular distributions for accelerated particles at a strong, weakly magnetized plane-parallel shock in the SAS limit. In this case, accelerated particles are defined as particles whose Lorentz factor far exceeds that of the shock, so that distribution characteristics in the injection domain are not traced. However, the injection process is modeled in Monte Carlo simulation approaches, and we show results probing this domain in later sections.

Figure 4 displays shock compression ratios and our Monte Carlo results for spectral indices and angular distributions at the shock in the NIF, for parallel shocks spanning a range of rapidities $\Gamma_1\beta_1$. Moreover, it exhibits corresponding results from Kirk et al. (2000) and clearly illustrates that we find excellent agreement between Monte Carlo simulation results and Figure 3 of their work. To facilitate comparison, we adopted the J-S EOS here, though we note that details of the shock parameters for Figure 3 of Kirk et al. (2000) were not explicitly stated in their paper. This is, effectively, a case approximating that of the red curve in Figure 2 here, save that $\Theta_{\rm Bf1} = 0^\circ$. This minor change actually simplifies the Rankine–Hugoniot solution and is shown as the solid black curve in the left panel of Figure 4. The spectral index σ is a monotonically increasing function of $\Gamma_1\beta_1$, as in Kirk et al. (2000) and Baring (2004), reflecting the increased energization per shock crossing cycle that competes against the influence of a declining compression ratio. The angular distributions in the right panel of the figure closely match those from Figure 3 of Kirk et al. (2000), all measured at the shock discontinuity. In this panel, $0 < \mu_s < 1$ cases are for particles heading downstream, and $-1 < \mu_s < 0$ are charges moving upstream. The distributions exhibit an increase in convective beaming downstream as the upstream flow speed increases. Such distributions were obtained as angle-dependent fluxes, and then divided through by the flux weighting factor $\beta\mu_s$ before normalization. This introduces the apparent statistical noise in the neighborhood of $\mu_s = 0$.

To delve deeper into the anisotropies incurred in relativistic shocks, in Figure 5 we examine the $\Gamma_1\beta_1 = 10$ case in more detail, extending the angular distribution illustrations to locations upstream (left panel) and downstream (right panel) of the shock front. Again the distributions correspond to high-energy particles with rapidity, $\gamma\beta \gg \Gamma_1\beta_1$. In each panel, the black histogram is the distribution function at the shock, exhibited in Figure 4. The origin of the shape of the angular distributions can be understood qualitatively. In non-relativistic shock scenarios, high-energy particles of speeds far in excess of that of the shock realize isotropy in all relevant frames of reference. However, in relativistic shocks, even particles traveling very close to the speed of light can no longer be considered isotropic in all relevant frames and at all positions. Consider a relativistic particle returning to the upstream side of the shock from the downstream side. The upstream fluid frame velocity vector of this particle is initially pointed upstream. As the trajectory is perturbed via SAS seeded by field turbulence, the velocity vector in the upstream fluid frame performs a random walk. Because of relativistic beaming effects,

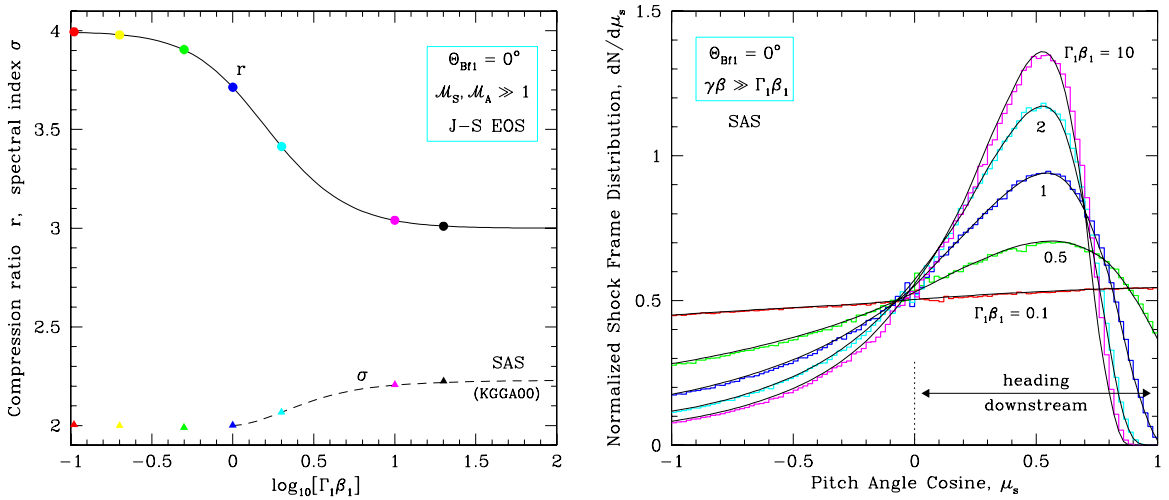

Figure 4. Left panel: the Rankine–Hugoniot MHD compression ratio r and spectral indices σ for non-thermal particle distributions, as functions of the shock rapidity $\Gamma_1\beta_1$, for plane-parallel, $\Theta_{Bf1} = 0^\circ$, shocks. The compression ratio is computed according to the protocols of Section 3. The points for r and σ correspond to select shock speeds with simulation data; most of these possess angular distributions illustrated in the right panel. The simulation runs were restricted to the SAS regime, for which the dashed curve corresponds to the low-magnetization semianalytic determinations of σ in Figure 4 of Kirk et al. (2000, labeled KGGA00). Right panel: NIF frame angular distribution functions, normalized to unity, for parallel ($\Theta_{Bf1} = 0^\circ$), relativistic shocks with bulk rapidities $\Gamma_1\beta_1$ as labeled, and compression ratios $r = 3.995$, 3.905, 3.714, 3.414, and 3.04, from lowest to highest speed (see points in left panel). Distributions were measured at the shock ($x = 0$) and sampled only high-energy particles with rapidity $\gamma\beta \gg \Gamma_1\beta_1$ in each case. The simulation results are the histograms, acquired for the small angle scattering (SAS) case, and the smooth curves are the semianalytic solutions that Kirk et al. (2000) obtained (see their Figure 3) to the diffusion-convection equation in the SAS limit.

(A color version of this figure is available in the online journal.)

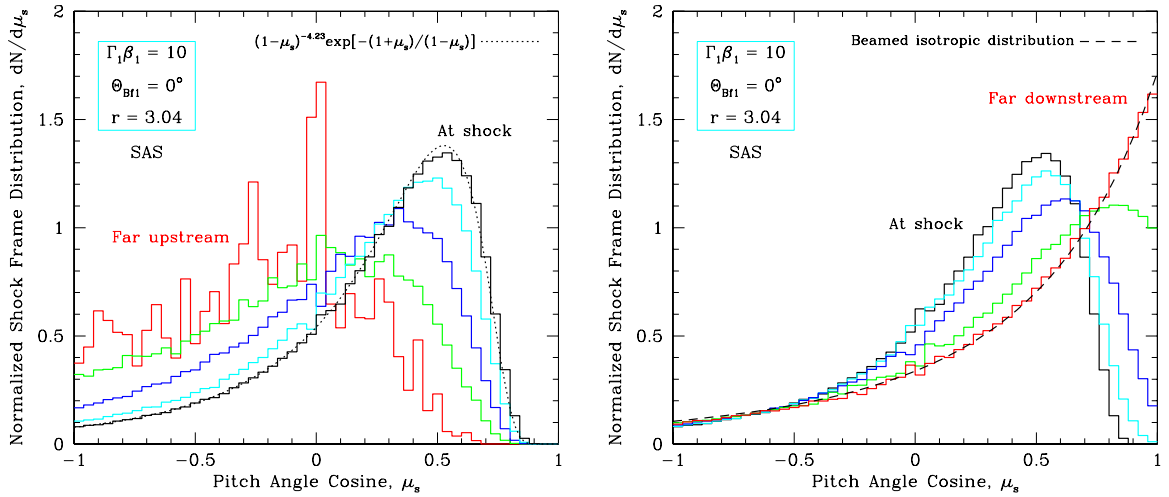

Figure 5. Normalized NIF frame angular distribution functions for high-energy particles with rapidity, $\gamma\beta \gg \Gamma_1\beta_1$, upstream (left panel) and downstream (right panel) of the shock at various distances. The simulation run was for a parallel ($\Theta_{Bf1} = 0^\circ$), ultrarelativistic shock with $\Gamma_1\beta_1 = 10$ and compression ratio $r = 3.04$, and diffusion in the SAS limit. Left panel: the black histogram is the distribution function at the shock and can be compared directly to the dotted line, which is an analytic result from Equation (23) of Kirk et al. (2000). The other four distribution functions are taken at increasingly large distances upstream of the shock. In units of $\Gamma_1\beta_1 m_p/qB$, the cyan curve is at $x = -20$, the blue curve at $x = -80$, the green curve at $x = -320$, and the red curve at $x = -1280$. Distribution functions determined at larger distances upstream suffer from poor statistics, since few particles are able to diffuse so far upstream against the relativistic flow. Right panel: as in the left panel, the black histogram is the distribution function at the shock, with the other histograms now corresponding to $x = 400$ (cyan), $x = 1600$ (blue), $x = 6400$ (green), and $x = 25600$ (red). The dashed line represents an isotropic distribution in the downstream fluid frame, as viewed by an observer in the NIF frame where the shock is stationary.

(A color version of this figure is available in the online journal.)

once the particle's path is perturbed by the small angle $\theta > 1/\Gamma_1$ in the upstream fluid frame, the shock frame x-component of the velocity (or angle cosine μ_s) becomes positive, sweeping the particle back to the shock before it has the chance to isotropize in the upstream fluid frame. Accordingly, the parameter space around $\mu_s = 1$ is underpopulated (actually exponentially suppressed) because the upstreaming particles have not had enough time to diffuse from $\mu_s < 0$ to $\mu_s \gtrsim 0.9$ before they are convected through the shock and downstream. This feature is critical to the hyper-efficient reflection in oblique relativistic shocks discussed in Section 4.2. Note that at various non-zero obliquities, similar NIF frame angular distributions are elicited in the simulation at the shock, but are not shown.

It is interesting to note that, as the particle detection plane is moved upstream, the domain of population suppression near $\mu_s = 1$ expands to lower μ_s. This is because particles that have angle cosines closer to $\mu_s \sim -1$ are more likely to penetrate further upstream, so that when diffusing outside the Lorentz cone, they are less likely to populate near $\mu_s \sim 1$. This skews the distribution progressively toward more negative μ_s. Additionally,

the probability of particles reaching a position x upstream exponentially declines with $|x|$ on diffusive length scales (e.g., see, Lee 1983; Summerlin & Baring 2006 for illustrations of this in non-relativistic, heliospheric shock contexts). Accordingly, distribution functions taken at larger distances upstream suffer from poor statistics. Thus, the upstream distribution functions exhibited in the left panel of Figure 5 are normalized to have the same area for display purposes.

The evolution of the distribution function downstream of the shock is shown in the right-hand panel of Figure 5, ranging from the distribution found at the shock (black histogram) to an isotropic distribution in the downstream plasma frame (red histogram). As the particles move downstream, the relativistic beaming that biases the distribution to higher average values of μ_s is progressively enhanced, and they eventually isotropize in the downstream fluid frame (the red histogram in the right panel). The dashed line in that panel is the angular (density) distribution function in the shock frame, $dN_s/d\mu_s$, for particles that are isotropic in the fluid frame with a power-law distribution $dN_f/dp_f \equiv 4\pi p_f^2 f(\vec{r},\, p_f) \propto p_f^{-\sigma}$. Here, $f(\vec{r},\, p_f)$ is the fluid frame phase space distribution function, which is Lorentz invariant. Hence, in the shock rest frame, the angular distribution satisfies $dN_s/d\mu_s \propto p_s^2\, p_f^{-(\sigma+2)}$ for a fixed choice of p_s, which is imposed on this example by truncating the NIF distribution at a lower limit of $p_s = p_0$. For ultrarelativistic particles, the relationship between p_s and p_f is given simply by the photon aberration formula $p_f = p_s\Gamma(1-\beta\mu_s)$. Accordingly, the angular distribution in the NIF for isotropy in the fluid frame scales as $dN_s/d\mu_s \propto (1-\beta\mu_s)^{-(\sigma+2)}$. This is what is illustrated in Figure 5, which for the $\Gamma_1 \gg 1$ case reduces to that for values $\beta \approx 1/3$ downstream and $\sigma = 2.21$.

This evolution of the anisotropy has consequences for the observed power-law index downstream of the shock. Because the average value of μ_s for the returning particles is lower than it would be for particles that are isotropized in the downstream fluid frame, the average bulk flow speed of the accelerated particles is lower than u_{2x}. As the angular distribution function diffusively evolves toward isotropy in the downstream fluid frame at larger x, the average velocity of the particles also increases, asymptotically approaching the higher bulk velocity of the downstream thermal particles. This necessarily reduces the density of the high-energy particles by conservation of particle number flux. The scale length for the evolution of the distribution function is approximately the particle mean free path. Thus, higher energy particles with typically longer mean free paths isotropize farther downstream than do particles of lower energy. Accordingly, the spectral shape of the distribution downstream of the shock evolves, illustrated in Figure 6, in a manner that correlates with the spatial changes in the angular distribution.

The black curve in Figure 6 displays the distribution function at the shock. However, just downstream (cyan curve), the low-energy particles have isotropized, thereby increasing their bulk flow speed and lowering their density, to conserve particle number flux. Higher energy particles in this curve have not yet fully isotropized and possess slightly slower bulk speeds and thus, higher densities. So, if one is measuring distributions somewhat downstream of a relativistic shock, the observed power law will be harder than the canonical $\sigma = -2.23$ result realized exactly at $x = 0$. At large distances downstream of the shock, accelerated particles of all rapidities far in excess of $\Gamma_2\beta_{2x}$ acquire the same beamed, isotropic distribution shown in the right panel of Figure 5, so that their cumulative density

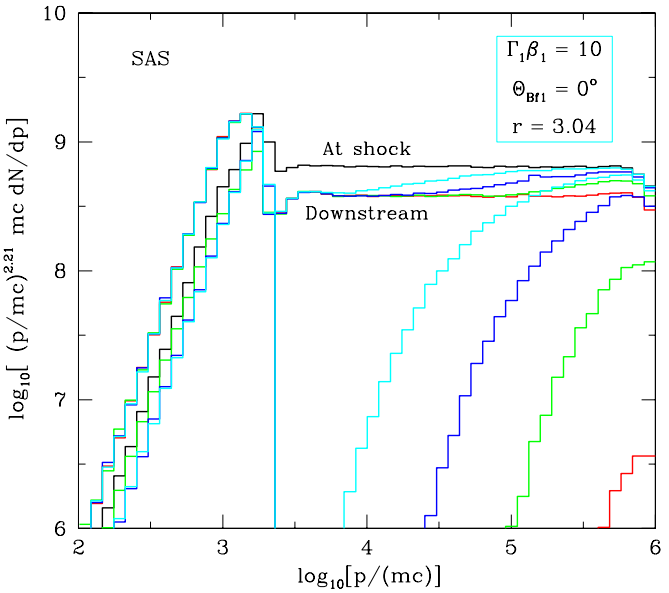

Figure 6. Accelerated particle distribution functions at positions upstream and downstream of the shock. The positions and color coding corresponding to Figure 5, with the histograms that fall sharply with decreasing momentum corresponding to the upstream positions, and the histograms that make only a small adjustment from the distribution function at the shock corresponding to downstream positions. To clearly illustrate the differences between these distribution functions, the differential density distribution dN/dp has been multiplied by $p^{2.21}$ so as to generate zero power-law slope at the shock. The paucity of low-energy particles at the upstream positions is due to their limited contraflow mobility, and is seen in non-relativistic shocks as the "convective peel-off" effect described in Summerlin & Baring (2006), see the text for a discussion. The spectral variations downstream of the shock are a result of energy-dependent density compression and are addressed in the text.

(A color version of this figure is available in the online journal.)

adjustments during downstream diffusion are identical, and the power-law index returns to that realized at the shock. This variation of the power-law index with the position of a downstream observer relative to the relativistic shock represents a fundamental shift from non-relativistic shocks, where the distribution function is isotropic in all relevant reference frames, and the spectral index is virtually independent of position when downstream of the shock. To our knowledge, this is the first time this effect in relativistic shocks has been highlighted in the literature.

4.2. Oblique, Subluminal Shocks

While small shifts in the power-law index can occur based on observation location and energy range in parallel shocks, the introduction of non-zero magnetic field obliquity creates more substantial ranges of power-law indices for the non-thermal particle component. In non-relativistic shocks, the power-law index is independent of magnetic field obliquity, and depends only on the compression ratio: $\sigma = (r+2)/(r-1)$ (Bell 1978; Drury 1983; Jones & Ellison 1991). In relativistic shocks, the spectral index varies dramatically with obliquity, as will be exemplified in due course. In particular, the character of the spectral index with respect to field obliquity hinges critically on whether the shock is subluminal or superluminal. Thus, our study of oblique relativistic shocks is divided into two sections to treat these parameter regimes separately.

Consider first subluminal, oblique shocks in the SAS limit. The first emphasis will be on the power-law behavior of the accelerated portion of the population; later on the injection

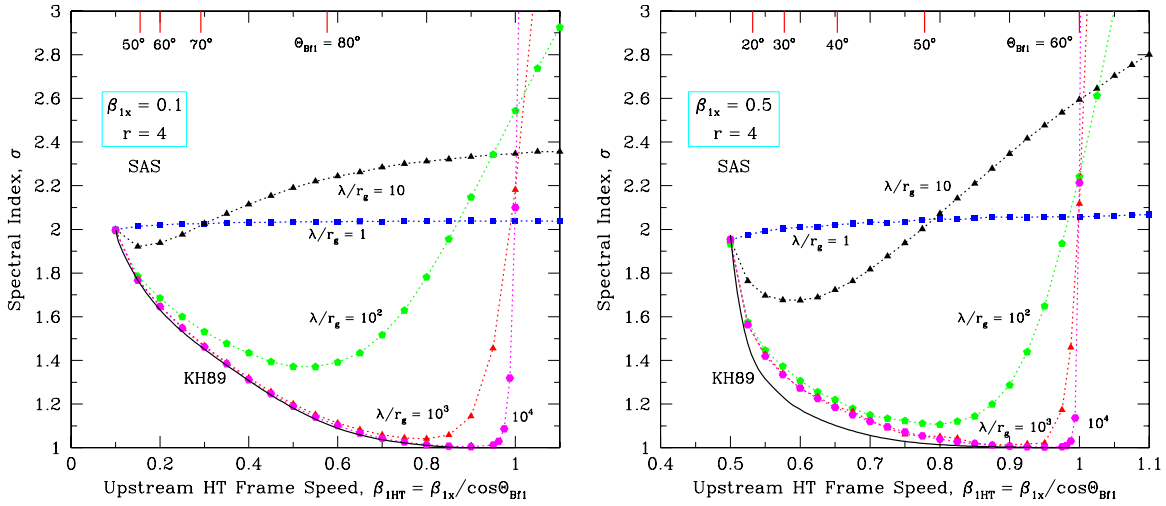

Figure 7. Power-law indices for simulation runs in the limit of small angle scattering (SAS), for an almost non-relativistic shock of upstream flow speed $\beta_{1x} \equiv u_{1x}/c = 0.1$ (left panel), and a mildly relativistic case with $\beta_{1x} \equiv u_{1x}/c = 0.5$ (right panel), for an MHD velocity compression ratio $r = u_{1x}/u_{2x} = 4$. The indices are displayed as functions of the effective de Hoffmann–Teller frame upstream flow speed $\beta_{1HT} = \beta_{1x}/\cos\Theta_{Bf1}$, with selected values of the fluid frame field obliquity Θ_{Bf1} marked at the top of the panel. Obliquities for which $\beta_{1HT} > 1$ constitute superluminal shocks. The displayed simulation index results were obtained for different diffusive mean free paths λ parallel to the mean field direction (see the text), namely, $\lambda/r_g = 1$ (blue squares), $\lambda/r_g = 10$ (black triangles), $\lambda/r_g = 10^2$ (green pentagons), $\lambda/r_g = 10^3$ (red triangles), and $\lambda/r_g = 10^4$ (magenta hexagons), as labeled. The lightweight black curve at the bottom labeled KH89 defines the semianalytic result from Kirk & Heavens' (1989) solution to the diffusion-convection equation, corresponding to $\lambda/r_g \to \infty$.

(A color version of this figure is available in the online journal.)

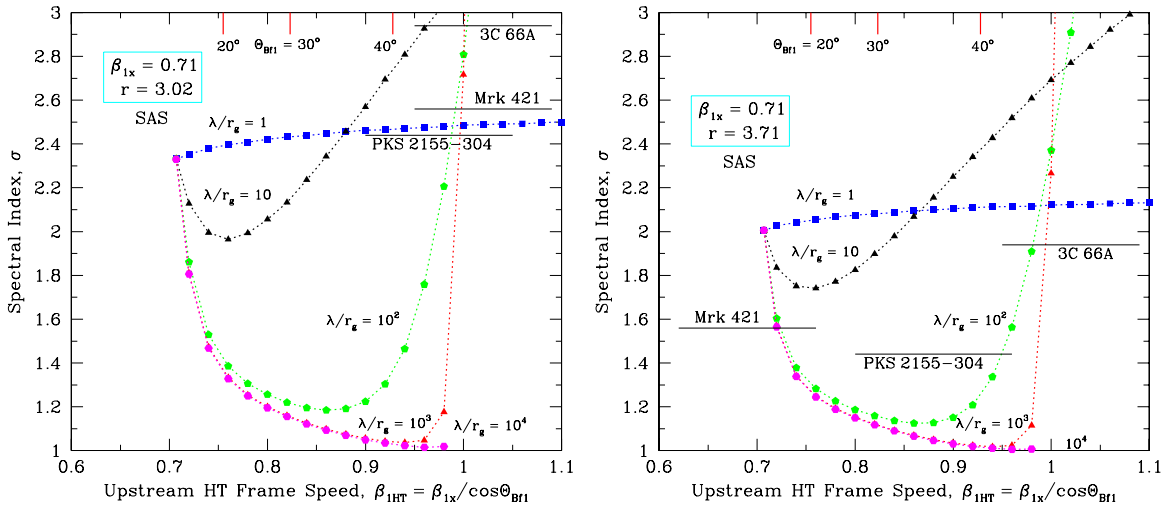

Figure 8. Power-law indices for simulation runs in the SAS limit, as in Figure 7, but now for shock parameters more appropriate to the internal shocks associated with the relativistic jets that are believed to be the source of GRBs. Here, $\beta_{1x} \equiv u_{1x}/c = 0.71$, and the compression ratio and sonic Mach number are now $r = u_{1x}/u_{2x} = 3.02$ and $\mathcal{M}_S = 2.6$ (left panel), and $r = u_{1x}/u_{2x} = 3.71$ and $\mathcal{M}_S = 60$ (right panel), calculated via the Rankine–Hugoniot relations derived in Section 3. The indices are again plotted vs. the effective de Hoffmann–Teller frame upstream flow speed $\beta_{1HT} = \beta_{1x}/\cos\Theta_{Bf1}$, and selected fluid frame field obliquities Θ_{Bf1} are as marked at the top. The different diffusive mean free path cases were again $\lambda/r_g = 1$ (blue squares), $\lambda/r_g = 10$ (black triangles), $\lambda/r_g = 10^2$ (green pentagons), $\lambda/r_g = 10^3$ (red triangles), and $\lambda/r_g = 10^4$ (magenta hexagons), as labeled. Also depicted are marker indices for three *Fermi* blazars, Mrk 421, 3C 66A, and PKS 2155-304; they apply for arbitrary β_{1HT}, and are truncated in the horizontal direction to aid clarity of the figure. These mark the approximate expectation for σ, uncertain to roughly ± 0.2, for an interpretation of the *Fermi*-LAT gamma-ray spectral indices as uncooled inverse Compton scattering (left panel) and strongly cooled upscattering (right panel); see Section 5 for a discussion.

(A color version of this figure is available in the online journal.)

efficiency will be addressed. In the simulation, for each run, the power-law regime is determined on an individual basis by inspection and can begin anywhere from 5 to 100 times the mean injection (i.e., approximately downstream thermal) energy. A least-squares fit in log–log space is used to determine the slope σ. Results are depicted in Figure 7 for $\beta_{1x} \equiv u_{1x}/c = 0.1, 0.5$, and in Figure 8 for $\beta_{1x} = 0.71$, for different values of the turbulence or cross-field diffusion parameter $\eta = \lambda/r_g$. The power-law index σ is plotted as a function of the HT frame dimensionless speed $\beta_{1HT} = \beta_{1x}/\cos\Theta_{Bf1}$. It is clear that there is a considerable range of indices σ for non-thermal particles accelerated in mildly relativistic, oblique shocks. The essence of this array of indices and the global trends with Θ_{Bf1} and η were outlined briefly in Baring & Summerlin (2009) and Baring (2011), though a fuller interpretation ensues below.

A feature of this plot is that the dependence of σ on field obliquity is non-monotonic. When $\lambda/r_g \gg 1$, the value of σ at first declines as Θ_{Bf1} increases above zero, leading to very flat spectra. As β_{1HT} approaches and eventually exceeds unity, this trend reverses, and σ then rapidly increases with

increasing shock obliquity as the shocks become superluminal. This dramatic steepening is a consequence of the inexorable convection of particles away downstream of the shock. The only way to ameliorate this rapid increase in index is to reduce $\eta = \lambda/r_g$ to values below around 10. Physically, this corresponds to increasing the hydromagnetic turbulence to high levels that force the particle diffusion to approach isotropy: $\kappa_\perp/\kappa_\parallel = 1/(1+\eta^2)$ in a kinetic theory description (e.g., Forman et al. 1974). This renders the field direction immaterial, and the shock behaves much like a parallel, subluminal shock in terms of its diffusive character. Note that this general character is also evinced in the very recent diffusion-convection equation analysis of Bell et al. (2011) at shocks of lower speeds. Figure 1 in their paper clearly illustrates that the distribution hardens with increasing obliquity when the shock is well within the subluminal regime and softens when the luminal boundary $\cos\Theta_{\rm Bfl} = \beta_{1x}$ is approached or crossed in quasi-perpendicular (and sometimes non-relativistic) shocks, unless the frequency of scattering is raised to the Bohm limit, for which the index then depends only weakly on the field obliquity.

In studying this case, we again choose to use previous semianalytic analyses as a benchmark for comparison: the work of Kirk & Heavens (1989, KH89 hereafter) is ideally suited for this purpose. KH89 calculated the spectral index of non-thermal particles at oblique, trans-relativistic shocks using the eigenfunction technique of Kirk & Schneider (1987) to solve the diffusion-convection equation. Their analysis was restricted to situations where particles do not diffuse across field lines, i.e., their collision operator contains only a pitch angle scattering term. They also assumed that particles conserve their magnetic moment on crossing the shock, a standard analytic simplification. Results from Figure 2 of their work are exhibited in Figure 7. Note that their exploration was done exclusively in the HT frame and was thus limited to subluminal shocks. An interesting product of their work was the appearance of power laws harder than both the non-relativistic and ultrarelativistic parallel shock results in Bednarz & Ostrowski (1998) and Kirk et al. (2000), achieved as $u_{1\rm HT}$ approaches the speed of light, but u_{1x} remains mildly relativistic. This is an idealized result, because the limit of zero cross-field diffusion does not occur in nature, since field turbulence abounds in astrophysical shocks, and is needed to drive acceleration. The Monte Carlo technique is ideally suited to examining how close to zero cross-field diffusion one must get to approach the particular analytical case explored by KH89. Figure 7 clearly indicates that when $\lambda/r_g \gtrsim 10^3$ the KH89 zero cross-field diffusion indices are closely reproduced for $\beta_{1x} = 0.1$ and well approximated for $\beta_{1x} = 0.5$. The physical origin for these extremely hard power laws will be discussed in Section 4.2.1.

To allow a direct comparison with the results of KH89, we adopted the same compression ratio of $r = 4$, and the same formulation for the relationship between the upstream and downstream magnetic fields. This formulation is found in Equations (2)–(4) of their work and is summarized below. It assumes a weak magnetic field that does not influence the plasma motion (i.e., $\mathcal{M}_{\rm A} \gg 1$); all the simulation runs used to generate Figure 7 satisfied this high Alfvénic Mach number criterion:

$$r = \frac{\beta_{1x}}{\beta_{2x}}$$
$$\frac{B_{1\rm HT}}{B_{2\rm HT}} = \sqrt{r^2 - \Gamma_1^2 (r^2-1)\,\beta_{1x}^2 \left[\frac{1}{\beta_{1\rm HT}^2} - 1\right]}. \qquad (33)$$

Given the upstream quantities above, and the compression ratio, r, we can solve for $B_{2\rm HT}$ and use our knowledge that B_x is constant across the shock along with an appropriate Lorentz transformation (see Section 3.2) to find the appropriate downstream value for B_z in any reference frame.

In Figure 7, while impressive agreement with the solutions of KH89 arises for $\beta_{1x} = 0.1$ when $\eta \gtrsim 10^3$, for $\beta_{1x} = 0.5$, we find that our simulation indices match the results of KH89 at $\beta_{1\rm HT} \gtrsim 0.5$ and just below $\beta_{1\rm HT} = 1$, but are noticeably softer (higher σ) in the central part of the curve. Increasing η as high as 10^6 creates no appreciable change in the resulting power-law index from that of $\eta = 10^4$: we believe that we have reached the asymptotic limit of our simulation. Monte Carlo results for $\beta_{1x} = 0.3$ are not depicted, but are similar to those for the $\beta_{1x} = 0.5$ case, and also exhibit a modest difference from the KH89 determinations of σ at intermediate values of $\beta_{1\rm HT}$, while matching at the $\beta_{1\rm HT}$ endpoints. We contend that the reason for the modest discrepancy between the two approaches probably lies in the assumption of conservation of magnetic moment employed by KH89. This assumption facilitates an analytic result but does not precisely describe orbiting particle reflection and transmission properties at an oblique shock discontinuity (see Terasawa 1979; Drury 1983; Pesses & Decker 1986 for non-relativistic shock expositions). For parallel or quasi-perpendicular (in this case nearly luminal) shocks, the magnetic moment is conserved, and the two approaches converge. For obliquities in between, there is slight non-conservation of magnetic moment, and the precise tracing of gyro-orbits in the shock layer, as is enacted in the Monte Carlo technique, introduces modest but appreciable increases in σ.

It is imperative to go beyond the artificial $r = 4$ exploration, since relativistic shocks are somewhat weaker in their compression. To this end we produced similar index plots for parameters more appropriate to internal shocks in GRBs and blazars using the Rankine–Hugoniot relations derived earlier. Specifically, Figure 8 displays Monte Carlo results for compression ratios that satisfy the J-S EOS, $\mathcal{M}_s = 2.6$ ($r = 3.02$) and $\mathcal{M}_s = 60$ ($r = 3.71$), with the Alfvénic Mach number assumed to be large. The results mirror those in Figure 7 in terms of overall character, with a large range of indices, $\sigma \sim 1$ in near-luminal cases when $\lambda/r_g \gtrsim 10^3$, and a rapid steepening of the non-thermal distribution in superluminal cases unless $\lambda/r_g \lesssim 10$. A particular index inferred from the radiation spectrum of a single astronomical source can be accommodated by a range of choices for shock speed, Mach numbers, field obliquity, and turbulence parameter η. This interpretative aspect is the subject of Section 5, with a focus on blazars.

Finally, note that Figures 7 and 8 were prepared specifically with diffusion seeded by gyroresonant interactions between charges and MHD turbulence in mind. In such cases, scattering descriptions are only physical if $\eta \geqslant 1$ in Equation (1), i.e., above the Bohm limit. Yet, $\eta < 1$ regimes for diffusion can be realized for non-gyroresonant interactions with field turbulence that is perhaps grown via filamentation or Weibel instabilities. Trial simulation runs were performed in this $\eta < 1$ domain, and it was found that the distribution was not very sensitive to the choice of η; for example, reducing η to 0.1 flattened the spectrum for the $\beta_{1x} = 0.71$, $\beta_{1\rm HT} = 0.96$, $r = 3.71$ case by an index of around 0.1 relative to that displayed in Figure 8. This behavior is a consequence of diffusion in this "sub-Bohm" domain resembling that for the Bohm limit of $\eta = 1$ for gyroresonant diffusion. A more complete exploration of this domain is deferred to future work.

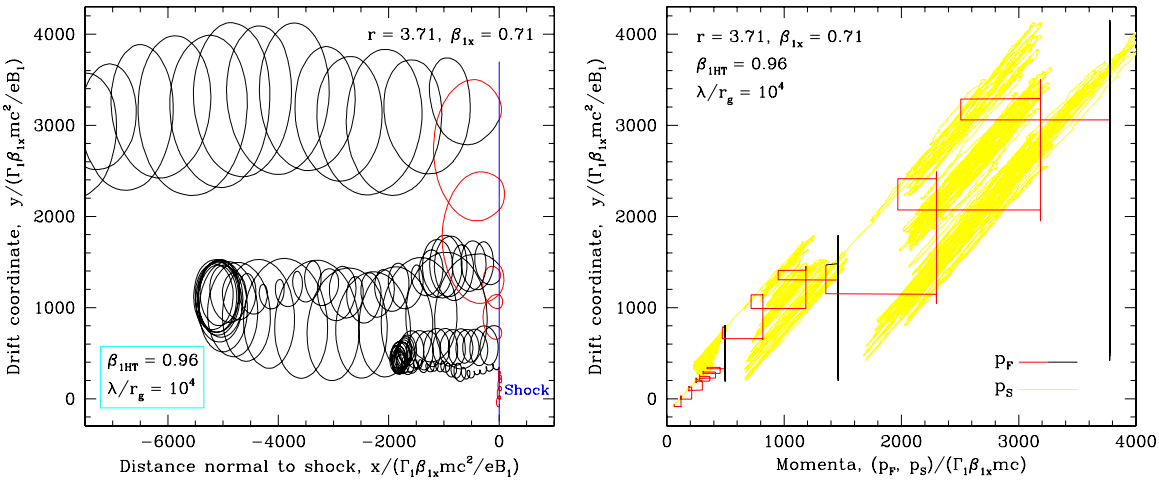

Figure 9. Left panel: a sample particle trajectory depicting strong SDA in an oblique mildly relativistic shock with de Hoffmann–Teller frame speed, $\beta_{1HT} = 0.96$, NIF shock speed, $\beta_{1x} = 0.71$, and compression ratio, $r = \beta_{1x}/\beta_{2x} = 3.71$ in a low-turbulence environment with $\lambda/r_g = 10^4$. The projection is onto the x–y plane, where the $\mathbf{u} \times \mathbf{B}$ drifts lie in the y-direction. This portion illustrates two key features of SDA: coherent trapping in the shock layer (colored red), interspersed with upstream excursions (black) after reflection via approximate conservation of magnetic moment. This particular particle gained orders of magnitude in energy before finding a pitch angle small enough to allow transmission and subsequent escape downstream. Right panel: the particle's position in the drift coordinate (y) direction, as a function of the magnitude of the momentum in the fluid frame, p_f, and the shock frame, p_s. This illustrates a core property of shock drift acceleration: that over large times both p_f and p_s display approximately linear trends with the drift y. Prolonged energy gains occur only during shock layer gyrations, when the fluid frame momentum exhibits a "rectangular hysteresis" (red). The shock frame momentum possesses perturbed oscillatory temporal behavior (yellow) during the intervening upstream excursions.

(A color version of this figure is available in the online journal.)

4.2.1. The Action of Shock Drift Acceleration

The bottom line of the preceding exposition is that the power-law index achieved in subluminal oblique shocks can be considerably less than even the $\sigma = (r+2)/(r-1)$ result for non-relativistic shocks. For moderate obliquities and $\eta = \lambda/r_g \gtrsim 10^3$ it can become as hard as $\sigma = 1$. A power law this hard can only be achieved in the case where particle escape from the acceleration region is miniscule. We illustrate here that the high η cases that have low σ are subject to strong SDA, offering a close examination of the trajectories of energized particles that reveals prolonged retention in the acceleration process. A small fraction of particles incident from upstream can be reflected at the shock because they have suitable pitch angles, and these seed the retention in the acceleration process. A sample trajectory and associated momenta for a select particle undergoing such acceleration is displayed in Figure 9. The particle was injected at superthermal energies to circumvent improbable injection from the thermal population, a property that is discussed later in this subsection. The trajectory highlights two hallmarks of SDA: coherent trapping in the shock layer, interspersed with upstream excursions after reflection at the shock (see Decker & Vlahos 1986 for illustrations in non-relativistic shock contexts). The reflection condition can be estimated by assuming conservation of magnetic moment in the HT frame, i.e., requiring that $(1-\mu_{p1}^2)/B_{1HT} = (1-\mu_{p2}^2)/B_{2HT}$, where μ_{pi} is the particle's pitch angle cosine in the upstream ($i = 1$) or downstream ($i = 2$) HT frame. This assumption is technically valid only when particles gyrate a large number of times in the shock layer (e.g., see Drury 1983), which arises when the gyroperiod is far inferior to the time it takes to convect one gyroradius downstream, i.e., when $p_s \gg \Gamma_1\beta_{1HT}$. For magnetic moment conservation, given $B_{2HT} > B_{1HT}$, it is clear that there are some values of μ_{p1} for which $\mu_{p1} \geqslant 0$ cannot be satisfied. In these cases, particles are reflected rather than transmitted, and the shock is acting as a magnetic bottleneck.

As particles gyrate in the shock layer, the work done dW on a charge can be computed using the Lorentz force, resulting in the equation

$$(mc)^2\,\gamma\,\frac{d\gamma}{dt} \;\equiv\; \mathbf{p}.\frac{d\mathbf{p}}{dt} \;=\; q\,\mathbf{p}.\left\{\mathbf{E}+\frac{\mathbf{v}}{c}\times\mathbf{B}\right\} \;\equiv\; q\,\mathbf{p}.\mathbf{E}, \quad (34)$$

where $\mathbf{E}$ is the $\mathbf{u}\times\mathbf{B}$ drift field. In the uniform $\mathbf{B}$ fields either upstream or downstream, the energy gains and losses acquired during a gyroperiod exactly cancel, so that no net work is done, $dW = mc^2 d\gamma = 0$. In contrast, when a charge's gyromotion straddles the shock discontinuity, it samples the different electromagnetic field on either side of the shock for different times, with the net acceleration on the upstream side of the shock being greater than the deceleration on the downstream side of the shock. Such an asymmetry in energy increments is explicitly evident in Equation (6) of Jokipii's (1982) exposition on SDA in non-relativistic shocks (see also Webb et al. 1983 for relativistic cases). This energization can be seen in the counterclockwise rotations of the p_f curve in Figure 9. In this curve, vertical motion indicates travel upstream or downstream of the shock where p_f is constant. The horizontal lines are shock crossings where the local p_f changes in transits of the shock discontinuity. By relating elapsed time during SDA to increments in the drift coordinate y, it is simply shown (Jokipii 1982) that

$$dW \;\equiv\; mc^2 d\gamma \;=\; qE_y\,dy \quad (35)$$

or $d(p/mc) \propto (eB_1/mc^2)\,dy$ in the relativistic limit of $\gamma \gg 1$. This energy gain scales linearly with displacement along y, with the proportionality constant depending on the shock obliquity. Such a linear scaling (in p_s) is the punch line of the right panel of Figure 9, where y effectively represents a time coordinate during shock drift episodes. This energization proportionality is clearly evident during shock interactions for the selected particle, and is an established hallmark of SDA. But notably, on larger scales, for both p_f and p_s, it is also an approximate description of the cumulative energization spanning multiple shock encounters.

This follows as a consequence of the constancy of p_f and only moderate changes to y during upstream excursions, i.e., material energy changes arise only during shock interactions. The p_s curve's behavior shows smooth and rapid energization during gyrations in the shock layer followed by a quasi-oscillatory epoch for p_s coupled with random spatial diffusion during the upstream excursions. The gradual increase of p_s during the upstream excursions results from the angular diffusion of the particle's fluid frame momentum vector in the upstream region. This increases p_s as the fluid frame velocity vector becomes more aligned with the flow vector. The widening of the gyrations in y is also due to angular diffusion gradually increasing the pitch angle upstream of the shock.

In typical SDA, a reflected particle gains energy and is sent back upstream to encounter the shock again. However, this alone cannot create such an unusually hard power law. In the case of non-relativistic shocks, this process happens commonly in oblique shocks when low levels of turbulence are assumed, with no impact on the power-law index: it still retains its $\sigma = (r+2)/(r-1)$ value (see Jokipii 1982; Lee 1984; Armstrong et al. 1985; Decker & Vlahos 1986; Webb et al. 1983; Pesses et al. 1982; Decker 1988; Vandas 2001). This is because the energy gained through SDA is exactly canceled by decreases in the efficiency of DSA in oblique shocks, since the angular distribution is effectively isotropic in the NIF and fluid frames. Furthermore, this isotropy guarantees that select particles are not trapped in the shock layer for long durations because they have the same probability of being reflected at each shock encounter. However, in the case of oblique subluminal shocks with HT frame speed approaching the speed of light, we find different circumstances.

As discussed in Section 4.1, in relativistic, parallel shocks in an SAS scenario, the field-aligned component of the distribution function is depleted at the shock. While the first shock encounter is that of an isotropic plasma boosted by the upstream flow speed with a strongly field-aligned population of particles, the distribution of particles returning after being reflected the first time is missing these field-aligned particles because the population has, in general, had insufficient time for any of them to become field aligned in the downstream direction before re-encountering the shock. This is a result of the fact that relativistic shocks preclude particle speeds from far exceeding the relevant flow speeds and becoming effectively isotropic in all reference frames. Subluminal, oblique relativistic shocks exhibit this same behavior. Upstreaming particles must initially have pitch angle $\mu_{\rm HT} \approx -1$ in order to travel upstream faster than the field line they are on is being convected downstream. Once they diffuse in pitch angle, they are quickly swept back into the shock before they achieve isotropy in the HT frame. Thus, as in the case of parallel shocks, the field-aligned, $\mu_{\rm HT} \approx 1$ component of the angular distribution function is depleted at the shock. Yet only such field-aligned particles are capable of penetrating the magnetic bottleneck at the shock. The net result of this dearth of field-aligned particles is a significant reduction in the fraction of particles transmitted through the shock at each encounter. This enhances the probability of reflection hardening the power law. As the HT frame speed approaches c, the transmission region can become completely depopulated leading to near 100% reflection and the observed $\sigma = 1$ power law.

The value of this index value is dictated by energy arguments. For long-lived trapping of select particles in the shock layer, energy in the particle population is transmitted from one Lorentz factor bin $[\gamma,\ \gamma + d\gamma]$ to the next one above, with miniscule loss. The energy content of this bin is γN, and when deposited in the next bin above, it is increased by SDA by an amount $\propto dy \propto d\gamma$ according to Equation (35), which is independent of the value of γ, but just on the electromagnetic structure of the shock layer. It then follows that the energy increment in going from adjacent bins is $\gamma dN \propto d\gamma$, so that $dN/d\gamma \propto 1/\gamma$, i.e., $\sigma = 1$. Introducing significant losses reduces this energy increment, and thereby steepens the spectrum. Along with the offering in Baring & Summerlin (2009), this is the first identification of the important role that SDA can play in determining the spectral index in relativistic shocks. In non-relativistic shocks, SDA does not influence the spectral index.

Note that the highly enhanced action of SDA is restricted to high η and SAS regimes. Invoking an LAS scenario completely eliminates the enhanced probability of reflection as particles are isotropic after their first upstream scattering and encounter the shock as such: all subsequent shock encounters have the same probability of reflection as the first shock encounter. For SAS scattering, increasing the amount of turbulence present (reducing η) allows particles to scatter into the transmission cone and subsequently softens the power law as shown in Figures 7 and 8. Trajectories for such $\eta \lesssim 10^2$ cases (not shown) exhibit a more "wonky" gyration and reveal prompt convection downstream, shutting down the opportunity for repeated episodes of coherent acceleration.

A few comments are necessary on the feasibility of encountering parameters that drive hyper-efficient SDA. The extremely large values of η required correspond to very low levels of turbulence that are not anticipated near shocks: it would require a truly unusual set of physical parameters to produce power laws significantly harder than $\sigma = 1.3$ using this mechanism. It should also be noted that the bulk thermal particles that create these strong shocks must be cold compared to the flow speed in order for the shock to form. Thus, despite the fact that they receive substantial kinetic heating during their first shock crossing, they will not meet the $p \gg \Gamma_1 u_{\rm 1HT}$ criterion and will have a reduced chance for reflection. Particles may have only a couple gyro-orbits that pass through the shock during an encounter and the range of phases that permit them to reflect is reduced dramatically. For $v < u_{\rm 1HT}$, it is physically impossible for particles to diffuse upstream along field lines, and some amount of cross-field diffusion is necessary for particles to return to the shock at all. This creates an injection problem; see Ellison et al. (1995) for a discussion of this in non-relativistic, oblique shock contexts.

One naturally asks how these energetic particles that so efficiently participate in SDA get accelerated to high energies in the first place. Figure 10 illustrates the injection problem for $r = 3.71$ shocks with very warm particles ($\mathcal{M}_{\rm S} = 4$). The distributions in these plots were used to determine the spectral slopes displayed in Figure 8 for each value of $\beta_{\rm 1HT}$. High-turbulence environments are clearly able to inject the particles efficiently, but the power law is steeper, namely, σ is higher. Low-turbulence environments have almost no injection until particles achieve $v > u_{\rm 1HT}$, at which point a strong, low σ power law develops as particles become trapped in the shock drift mechanism. This becomes particularly pronounced in the $\beta_{\rm 1HT} = 0.96$ case, an almost luminal shock situation, where convection of thermal upstream particles through and downstream of the shock is extremely rapid. The rapid decline of injection efficiency with η is an important factor in interpreting the action of shock acceleration in astronomical sources, an issue discussed in Section 5.

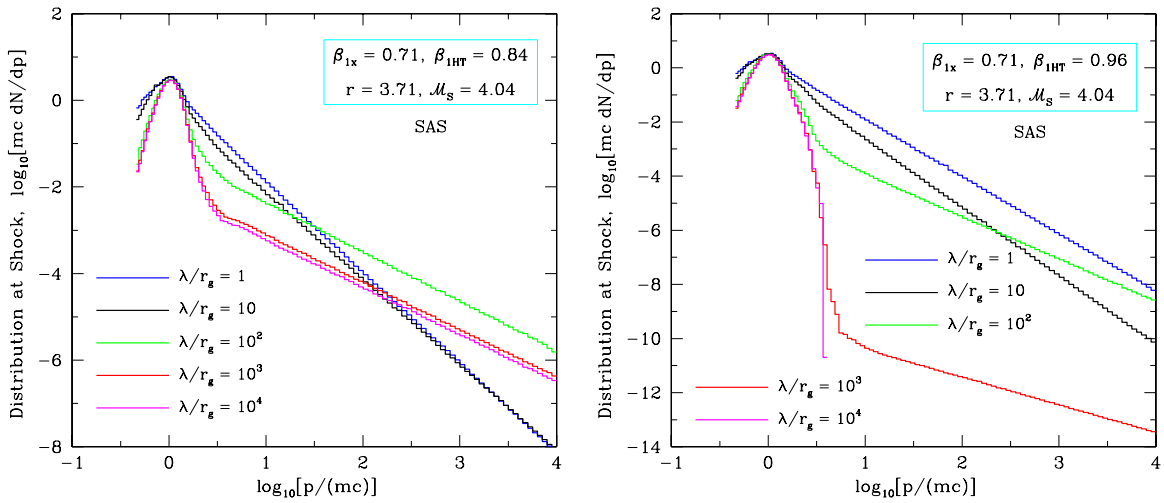

Figure 10. Full particle distributions for simulation runs in the small angle scattering (SAS) limit, for the strong mildly relativistic shocks of upstream flow speed $\beta_{1x} \equiv u_{1x}/c = 0.71$ whose indices are displayed in Figure 8. Here, the de Hoffmann–Teller frame upstream flow speed was set at $\beta_{1HT} = 0.75$ ($\Theta_{Bf1} \approx 48.^\circ 2$), and the five values of the diffusive mean fee path $\lambda/r_g = 1, 10, 10^2, 10^3, 10^4$ correspond to those in Figure 8—the color coding of the distributions and the spectral index results in the respective figure coincides. The velocity compression ratio was fixed at $r = u_{1x}/u_{2x} = 3.71$, and the upstream temperature corresponded to a sonic Mach number of $M_S = 4.04$ ($T = 5.45 \times 10^7$ K for an e^- to e^+ shock).

(A color version of this figure is available in the online journal.)

4.3. Oblique, Superluminal Shocks

In superluminal shocks, it is physically impossible even for particles moving at the speed of light to diffuse upstream along the field lines. Without any cross-field diffusion, the particles are inexorably swept downstream after passing through the shock without reflection, regardless of their energy; see Begelman & Kirk (1990) for illustration of such trajectories. Thus, the particles in the low-turbulence environment that relied on reflection for retention in the system are lost and not accelerated. Consequently, the power law becomes very soft. Particles in high-turbulence environments are not truly affected by the change in the obliquity of the magnetic field because they can travel across field lines as easily as they can along them. It is generally found that for $\beta_{1HT} < 1$ decreased turbulence enhances acceleration in the power-law tail, and for $\beta_{1HT} > 1$, the opposite holds. This result adds new perspective to the paper by Ellison & Double (2004), which presented results showing that the power-law tail indices in ultrarelativistic ($\Gamma_1 \gg 1$) shocks are extremely sensitive to both η and the obliquity of the magnetic field, with the power-law index increasing sharply as these parameters increase. These dependences are also seen in the mildly relativistic shocks discussed here, but with somewhat less sensitivity to η and Θ_{Bf1}.

While it is clear that an increase in η will soften the power law in oblique, superluminal shocks, the exact values of the power-law index are simulation dependent. Therefore, it is prudent to compare our results with those of Ellison & Double (2004, hereafter ED04). The code used in ED04 is a Monte Carlo simulation that is algorithmically very similar to the simulation presented in this paper. However, the simulations were developed independently and can each serve as an objective test of the other. For non-relativistic shocks, both simulations find the standard results of $\sigma = (r + 2)/(r - 1)$, where r is the compression ratio of the shock and σ is defined such that $dn/dp = p^{-\sigma}$. In the case of ultrarelativistic, parallel shocks, both simulations also find the theoretical results $\sigma = -2.23$. In the regime of oblique, relativistic shocks, ED04 focused predominantly on superluminal cases of high Mach numbers, with high levels of turbulence near the Bohm diffusion limit.

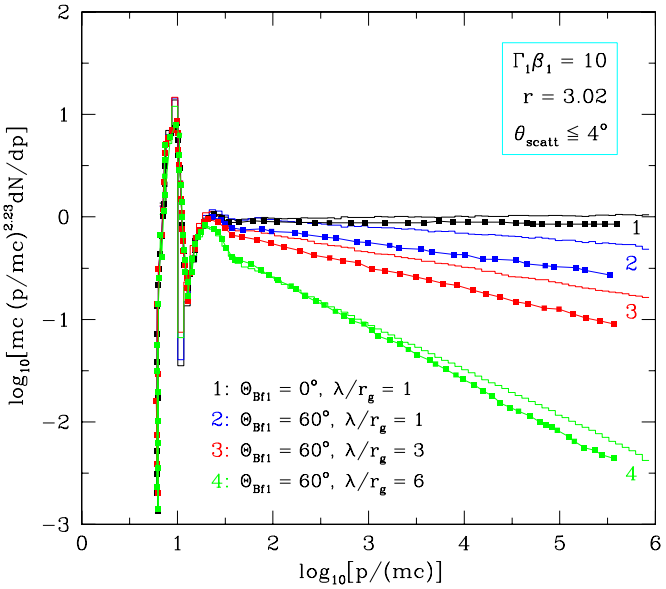

Figure 11. Direct comparison between distribution results from our simulation, the histograms, and those Ellison & Double (2004), the solid lines, for a relativistic shock with upstream Lorentz factor $\Gamma_1 = 10$ and compression ratio, $r = 3.02$, for different values of the upstream magnetic field obliquity, Θ_{Bf1}, and $\eta = \lambda/r_g$, the turbulence parameter. Specifically, the results from the top panel of their Figure 7 are compared here with the y-axis multiplied by $p^{4.23}$ to match the presentation in that figure. Both simulations identify the same trends with only minor differences in the value of the power-law slope.

(A color version of this figure is available in the online journal.)

In Figure 11, we compare results from our simulation (histograms) to the results from the top panel of Figure 7 in ED04 (solid lines) for a relativistic shock with upstream $\Gamma_1 = 10$ and compression ratio, $r = 3.02$, for different values of the upstream magnetic field obliquity, Θ_{Bf1}, and $\eta = \lambda/r_g$. Both sets of results are in the SAS limit, with the Rankine–Hugoniot solutions for the MHD shock obtained using the prescription of Double et al. (2004), as outlined in ED04, as opposed to the J-S EOS scenario; see Section 3.3 for details. For $\Theta_{Bf1} = 0°$, both simulations produce a result very close to the canonical $\sigma = -2.23$

power law (note that the y-axis is multiplied by $p^{2.23}$ such that a horizontal line is the canonical result). However, at $\Theta_{Bf1} = 60^\circ$, $u_{1x}/\cos\Theta_{Bf1} \approx 2$, making the shock decidedly superluminal. Thus, cross-field diffusion is essential in order for particles to be able to return to the shock and increasing η increases the power-law index considerably. This trend is identified by both simulations in this $\eta \lesssim 6$ domain; in our simulation it continues to somewhat higher η before statistical degradation inhibits determination of the spectrum. In general character, results from the two simulations are clearly similar, and numerically they are close. Yet there is a real difference, with the index determination differing between the two sets of results within the range of 1%–2%. The numerical precision of σ in our simulation is of the order of 1%. Comparisons were made with other superluminal shock results published in ED04, finding similar levels of agreement. The origin of the small spectral differences evinced in Figure 11 is not yet clear; we believe that the thorough comparison of our indices and angular distributions with the semianalytic approaches of Kirk & Heavens (1989) and Kirk et al. (2000), among other simulation checks, advocates for the robustness of our results.

The simulation developed by Niemiec & Ostrowski (2004, hereafter NO04; see also Niemiec & Ostrowski 2006) provides another opportunity for comparison. NO04 use a fundamentally different mechanism for particle scattering from our Monte Carlo simulation. Instead of phenomenologically scattering particles and specifying a momentum dependence for the mean free path, their simulation injects a prescribed spectrum of turbulent magnetic field structure that is superposed on the bulk magnetic field. Variations in the magnetic field perturb the gyro-orbits of the particles and are intended to mimic turbulence that a particle might encounter. Because NO04 use a turbulent magnetic field, particle trajectories must be integrated over much shorter time steps than is possible in the Monte Carlo code presented in this paper. This necessarily results in longer run times and poorer statistics. These poor statistics are particularly evident in the angular distributions produced in Figures 4, 8, and 11 of their work. We find qualitatively similar general behavior for results from the two techniques.

Consider Figure 2 of NO04, where distribution functions for accelerated particles in subluminal, mildly relativistic oblique shocks with compression ratio, $r = 5.11$ are exhibited. This value of r exceeds the non-relativistic, strong shock limit of $r = 4$, and is appropriate for the mildly relativistic electron–proton shocks studied in Heavens & Drury (1988), from whom they acquired their compression ratios. Though there is not a simple relationship between the two turbulence parameters ($\delta B/B$ in their work and η in our simulation), they are correlated with low values of $\delta B/B$ corresponding to high values of η. In subluminal shocks for small $\delta B/B$, the power-law index for the distribution function, $f(p)$, which they call α, is approximately 3. This is related to the power-law index for the differential density distribution by $\sigma = \alpha - 2$ or $\sigma \approx 1$ in their low-turbulence limit. This agrees with both our results and those of KH89. Additionally large amounts of turbulence soften the power law as we observed in our simulations runs. Finally, it is interesting to note that at high energies, where particles are resonant with wavelengths larger than the stirring scale of their simulation, turbulence disappears for particles at these energies ($\eta \to \infty$) and the power law becomes $\sigma = 1$, in good agreement with our results. In superluminal oblique shocks such as those shown in Figure 5 of their paper, although the statistics are somewhat poor, it is clear that low turbulence is no longer an asset to the acceleration process. In the shocks shown there, the power law is consistently softer in the low-turbulence cases, and in some cases no acceleration occurs without significant turbulence. In the high-turbulence case, power laws are still produced, but then the definition of the shock obliquity and the details of particle diffusion become more important in determining the resulting power-law index, rendering comparison with our results less insightful.

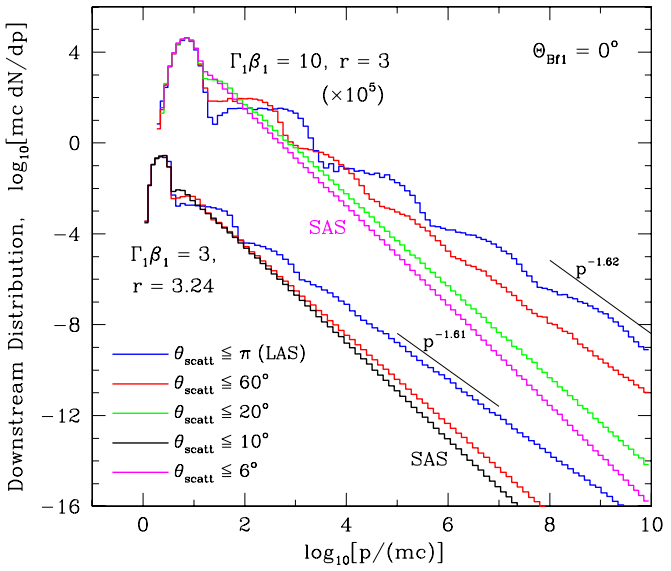

Figure 12. Particle distribution functions dN/dp from parallel shocks that are either mildly relativistic ($\Gamma_1\beta_1 = 3$, i.e., $\beta_1 = u_1/c \approx 0.949$) or ultrarelativistic ($\Gamma_1\beta_1 = 10$, i.e., $\beta_1 = u_1/c \approx 0.995$; multiplied by 10^5 to effect clarity of depiction), of velocity compression ratios $r = u_1/u_2 \approx 3.24$ and $r \approx 3$, respectively. For these simulation runs, scattering off hydromagnetic turbulence was modeled by randomly deflecting particle momenta by an angle within a cone of half-angle θ_{scatt}, whose axis coincides with the particle momentum prior to scattering. Values of θ_{scatt} span the range from large angle scattering (LAS: $\theta_{scatt} \leqslant \pi \gg 1/\Gamma_1$) to small angle scattering or pitch angle diffusion, when $\theta_{scatt} \lesssim 1/\Gamma_1$ and the distributions become independent of the choice of θ_{scatt}. All distributions asymptotically approach power laws $dN/dp \propto p^{-\sigma}$ at high energies. For two LAS cases, these power laws are indicated by lightweight lines, with indices of $\sigma = 1.61$ ($\Gamma_1\beta_1 = 3$) and $\sigma = 1.62$ ($\Gamma_1\beta_1 = 10$).

(A color version of this figure is available in the online journal.)

4.4. Large Angle Scattering Domains

One aspect of the simulation parameter space that has been neglected until now is the impact of varying the microphysics of the turbulent interactions; all previous results have focused on the SAS limit. In this section, we explore such using our Monte Carlo simulation to model relativistic parallel shocks, by varying θ_{scatt}, the angular width of the conical sector into which the particle's momentum vector is scattered at each encounter with magnetic turbulence. A value of $\theta_{scatt} = \pi$ corresponds to LAS, where the particles scatter ~1 time per mean free path; this is the domain first highlighted by Ellison et al. (1990a). A small value corresponds to SAS, where the particles scatter N times per mean free path, where N is given by Equation (2).

Figure 12 depicts accelerated particle distributions for two different shock speeds, illustrating the multitude of power-law indices available while varying only the scattering angle, θ_{scatt}, and fixing the obliquity at $\Theta_{Bf1} = 0^\circ$. Observe that for such parallel shocks, the distributions are independent of the diffusion parameter η since they are measured just downstream of the shock. This depiction complements results published in Figure 2 of Stecker et al. (2007) and illustrates two primary

results. The first is that LAS scattering produces a step-like structure in the accelerated distribution, a characteristic first identified by Ellison et al. (1990a). Each step corresponding to particles with increasing numbers of shock transits. In other words, the first step consists almost entirely of particles that have crossed the shock three times. Particles in the second step have almost all crossed the shock five times, etc.; see Baring (2004) for an illustration of this correlation. The precise correlation between shock transit number and particle energy weakens as the structure damps into a power law. The prevalence of the step structure, and how high in energy it extends before relaxing into a power law, increases with the Lorentz factor Γ_1 of the shock.

The second major result is that decreasing the scattering angle removes this structure but at the same time, softens the resulting power law. A complete investigation of why the power law is harder in the LAS scenario is deferred to future work, yet the origin of this trend in $\theta_{\rm scatt}$ centers on the distribution function at the shock. While LAS produces a beamed isotropic distribution similar to the red histogram of the right panel of Figure 5 at the shock, SAS generates a distribution like that shown in the black histogram of the same panel. Both the probability of return to the shock from the downstream side, and the energization per shock crossing, are functions of this angular distribution function (Bell 1978; Peacock 1981; Blasi & Vietri 2005). For non-relativistic shocks, the distribution function is necessarily isotropic to leading order, which restricts the power-law index to be only a function of the compression ratio. Relativistic beaming is the probable cause for breaking this degeneracy in $\theta_{\rm scatt}$ space. Evolution of the angular distribution with $\theta_{\rm scatt}$ can be inferred from Figure 6 of Blasi & Vietri (2005). Note that introducing magnetic field obliquity can alter the nature of this trend, as is indicated in Morlino et al. (2007). Future work will explore the variation of asymptotic values of the index σ as functions of $\theta_{\rm scatt}$ and $\Theta_{\rm Bf1}$, and also compare the Monte Carlo simulation values with those obtained from the semianalytic, transport equation approach of Blasi & Vietri (2005) and Morlino et al. (2007).

5. OBSERVATIONAL CONNECTION: THE IMPACT ON BLAZAR GAMMA-RAY INTERPRETATION

To briefly outline how these simulation results are relevant to astrophysical contexts, we discuss blazars, the subset of AGNs possessing relativistic jets of material emanating from the supermassive black holes at their centers; these jets are oriented virtually toward the observer. Blazars were discovered as a class of gamma-ray sources by the EGRET experiment on the *Compton Gamma-Ray Observatory* (Hartman et al. 1992), and subsequently detected by ground-based Çerenkov telescopes at TeV energies (Punch et al. 1992). The EGRET blazar measurements have been built upon in the last three years by *Fermi* Large Area Telescope (LAT) detections of dozens of blazars, offering improved spectroscopy. The TeV-band signals typically exhibit steep photon spectra (e.g., see, Krennrich et al. 2002; Aharonian et al. 2003 for observations of Mrk 421) that include the absorption due to pair producing interactions $\gamma\gamma \rightarrow e^+e^-$ with infrared and optical light generated by the intergalactic medium along the line of sight to the observer. Extremely flat particle distributions are inferred in some blazars after correcting for this attenuation (see, for example, Stecker et al. 2007), with indices as low as $\sigma \lesssim 1.5$ in high-redshift sources. Coupled with the TeV-band capability, the *Fermi*-LAT detections of blazars enable refined diagnostics by extending the observational window over a much larger energy range, and most crucially, including below the $\gamma\gamma \rightarrow e^+e^-$ attenuation window. Accordingly, *Fermi* observations can probe more directly the underlying radiating particle population. The implications of this we explore here. The reader can consult Baring (2011) and references therein for the interpretation of relativistic shock acceleration in GRB contexts.

Pertinent blazar data from the *Fermi*-LAT and TeV telescopes can be found in the GeV–TeV blazar "compendium" in Abdo et al. (2009). There is also the more extensive AGN catalog of *Fermi* in Abdo et al. (2010). For the purposes of discerning indices σ of particle populations generating the gamma-ray emission, it is important to consider photon spectra below any turnovers that may appear in the LAT band. This biases the data selection to below 1 GeV, and a nice tabulation of this for *Fermi*-LAT blazars is given in Tables 5 and 6 of Abdo et al. (2009). Therein, and in the various spectral plots given in that paper, it is clear that there is a modest spectral steepening above around 1 GeV in around 50% of *Fermi*-LAT blazars; this becomes much more pronounced above 100 GeV. From this data compilation, we use photon indices of $\alpha_\gamma = 1.72$ for PKS 2155-304, $\alpha_\gamma = 1.78$ for Mrk 421, and $\alpha_\gamma = 1.97$ for 3C 66A, as a sample blazar selection. The uncertainties on these indices are of the order of ± 0.1, which propagate into inferred particle indices σ. Note that a sizable fraction of LAT-band AGN indices in the catalog of Abdo et al. (2010) fall below $\alpha_\gamma \sim 2$, so that our choice here is reasonable. Note also that 3C 279 is considerably steeper in the LAT window, which could be a signature of a low-energy onset of the spectral turnover, or the operation of the Klein–Nishina regime of inverse Compton scattering.

Consider first a standard leptonic model interpretation of blazar emission as emanating from inverse Compton scattering by shock-accelerated electrons upscattering low-energy photons. The relationship between the particle index σ and the photon one is then $\sigma = 2\alpha_\gamma - 1$ (e.g., see chapter 7 of Rybicki & Lightman 1979), if there is insignificant radiational cooling. This applies to synchrotron self-Compton scenarios, where a single population of electrons emits the synchrotron radiation that it then upscatters to the gamma-ray band, or to an external supply of seed photons. For our select blazars, these indices fall in the range $2.44 < \sigma < 2.94$ and are marked on the left panel of Figure 8. They have an uncertainty $\Delta\sigma \sim \pm 0.2$. From this it is clear that for shock layer diffusive scattering in the SAS regime, acceleration at mildly superluminal oblique shocks provides a good description for all three of the blazars. This requires strong scattering, $\lambda/r_g \lesssim 10$. If $\lambda/r_g \lesssim 2$, i.e., near the Bohm diffusion limit, then Mrk 421 and PKS 2155-304 could be modeled with subluminal shocks.

In contrast to this, consider an alternative picture of "strong cooling" by inverse Compton scattering (or synchrotron radiation). This corresponds to rapid acceleration of the leptons at shocks, followed by convection and diffusion away downstream into a larger radiative zone where the gamma-ray signal is generated over longer timescales. Then, as is well known, the time-averaged effective electron distribution that radiates is a power law of index $\sigma + 1$ (e.g., see, Blumenthal 1971 for an analysis). The steepening reflects a pileup at lower Lorentz factors γ_e induced by the fact that the energy loss rate for both synchrotron and inverse Compton cooling of electrons scales as γ_e^2. The consequence is that now the relationship between the particle index σ and the photon one is $\sigma = 2\alpha_\gamma - 2$. These indices are marked on the right panel of Figure 8, and exhibit a shift of unity down from those in the uncooled case. Again, they have an uncertainty $\Delta\sigma \sim \pm 0.2$. Now, subluminal

regimes are clearly suggested, and in the cases of Mrk 421 and PKS 2155-304 move the inferences into $\eta = \lambda/r_g > 10$ territory. This opens up the question of whether such weak turbulence can persist in a blazar jet shock. However, there is considerable uncertainty in the spectral data, and increasing the scattering angle $\theta_{\rm scatt}$ somewhat above the SAS limit will reduce the value of η required to generate a particular value of σ.

These inferences should be viewed only as general guidelines, modulo the uncertainties in σ spawned by the precision of *Fermi*-LAT spectral index determination. We have selected one particular shock speed β_{1x} and restricted the discussion to SAS regimes. Clearly, there is a range of shock speeds, field obliquities, scattering angles $\theta_{\rm scatt}$, and turbulence parameters η that can satisfy a measured gamma-ray index. In addition, this discussion has focused on leptonic models; in hadronic ones mediated by pion decay, α_γ generally approximately traces the particle index σ, mimicking the situation in the right panel of Figure 8. Significant Klein–Nishina modifications to the spectrum in the LAT window can further complicate the interpretation. While more extensive study can hone the parameter space, broader gamma-ray coverage below 100 MeV and multiwavelength modeling are necessary to make significant strides. The multiwavelength aspect is more immediate in terms of its possibilities. For example, if the acceleration at the shock is limited by synchrotron cooling in controlling the maximum electron Lorentz factor, then the turnover in the synchrotron component is at an energy of $\sim m_e c^2/(\alpha_{\rm f}\eta)$ (for $\alpha_{\rm f} = e^2/\hbar c$ as the fine structure constant), a well-known result that is discussed in Garson et al. (2010) with reference to Mrk 421. Evidently, this energy must match that seen in hard X-ray/soft gamma-ray observations, providing additional constraints on η that often may not be near the Bohm limit of $\eta = 1$. This illustration serves to motivate future multiwavelength models of blazar spectra using complete distribution functions from acceleration simulations like those presented in this paper.

6. CONCLUSIONS

This paper has presented new results from a robust Monte Carlo simulation that complement and extend previous semi-analytic and computational results. It employs the simulation technique devised by Ellison et al. (1981) that was extended to relativistic shocks by Ellison et al. (1990a). The simulation produces steady state distribution functions for planar shocks of infinite extent for large ranges of shock speeds, energies, and positions, simulating both the injection and acceleration of particles via first-order DSA. By using the unique advantages that a simulation has over semianalytic, diffusion-convection equation solution techniques, we are able to expand upon the work of previous authors by examining various turbulence regimes and probing individual particle trajectories. This affords specific insights that cannot be gleaned from idealized cases that are analytically tractable. Our body of results leads to several key conclusions.

1. The power-law index in relativistic shocks samples a considerable range of values, and depends critically on the nature and magnitude of turbulence, the shock speed, and the shock field obliquity. This range extends from extremely hard power laws with $\sigma \approx 1$ to extremely steep distributions where simulation statistics preclude discernment of acceleration beyond the thermal injection domain. Notably, ultra-relativistic shocks do not necessarily possess the "canonical" $\sigma \approx 2.23$ power-law distribution, a result evident in the previous works of Kirk & Heavens (1989), Ellison & Double (2004), and Stecker et al. (2007).
2. When SAS is invoked, the value of $u_{1x}/\cos\Theta_{\rm Bf1}$ defines a critical division point in the parameter space. When it is less than c, oblique shocks in low levels of turbulence accelerate high-energy particles extremely efficiently via SDA, but when this quantity is greater than c, turbulence becomes vital to injection and acceleration in oblique, superluminal shocks. In both cases, weak levels of turbulence strongly inhibit injection from the thermal population.
3. Invoking LAS produces significant structure in the high-energy particle distributions in relativistic shocks, a phenomenon first identified by Ellison et al. (1990a), but also generates slightly harder distributions than a similar shock in the SAS scenario, where there is only a power law with little discernible structure.

These results represent important advances for determining the nature of turbulent shock environs in blazar and GRB jets, and in other astrophysical objects. Such interpretations are, admittedly, complicated by the particular spatial environment and radiation emission mechanism chosen for generating the observed photon spectra from these sources. However, global insights such as deciding between subluminal or superluminal shock environments are now possible.

To develop our model to aid future interpretations of astrophysical shocks, additional details of shock physics will be incorporated into the simulation. In shocks such as those discussed above with $\sigma < 2$, a majority of the energy in the system will be found in the accelerated particles. The Rankine–Hugoniot jump conditions for the shock must then be modified, since a step function shock profile is no longer a valid approximation. This yields a nonlinear acceleration phenomenon that is already seen clearly in Earth's bow shock, models of supernova remnant shocks, and the heliospheric termination shock (e.g., Ellison et al. 1999). Additionally, while this paper worked primarily with large Alfvénic Mach number shocks, in principle, low Alfvénic Mach numbers are possible in jet systems as well. While the Rankine–Hugoniot solutions presented above are fully capable of determining the appropriate jump conditions, low Alfvénic Mach number shocks may produce significant second-order Fermi acceleration due to the motion of the scattering centers (Alfvén waves) in the upstream and downstream rest frames. The code currently assumes scattering centers that are stationary in their respective fluid frames but can easily be adapted to include non-stationary scattering centers for the case of low Alfvénic Mach number shocks. In addition, preliminary work has also been done laying the ground work for future inclusion of cross-shock potentials in the simulation (Baring & Summerlin 2007). The simulation is currently a single fluid model, treating electrons/pairs or ions. For electron–proton shocks, the disparate diffusion scales of the two species will cause their distribution functions to react to the presence of the shock on different length scales. This charge separation at the shock discontinuity induces an electric field that acts to restore quasi-neutrality, and can lead to significant energy exchange between ions and electrons. The inclusion of these effects and the determination of their impact on injection and acceleration of protons and electrons will be the focus of future work.

We thank the anonymous referee, and Don Ellison and John Kirk for some comments helpful to the polishing of the manuscript. M.G.B. is grateful for the generous support of the NASA Astrophysics Theory and Heliospheric Physics

Programs through grants NNX10AC79G and NNG05GD42G, and the National Science Foundation through grant PHY-0758158. M.G.B. is also grateful to the Kavli Institute for Theoretical Physics, University of California, Santa Barbara for hospitality during part of the period when this research was performed, a visit that was supported in part by the National Science Foundation under grant No. PHY05-51164.

APPENDIX

THE ANGULAR DISTRIBUTION OF PARTICLES AT THE RETURN PLANE

Downstream of the shock, once the particle distribution has realized isotropy in the local fluid frame at some position x, it maintains isotropy as an asymptotic state at all positions further downstream. Tracking diffusion downstream of x to assess the momentum components of particles that return to position x is CPU intensive. A much faster method is to compute the probability of return to x and these momentum components statistically, subject to the condition of isotropy in the local fluid frame, and constancy of the returning particle's fluid frame momentum p_f. This was the expedient approach of Ellison et al. (1990a). In this appendix, we develop the formalism for angular distributions of returning particles for *arbitrary* p_f, not just ultrarelativistic particles, as has been the restriction of previous expositions. At x, the flow speed will be βc, i.e., of Lorentz factor Γ (subscripted 2 in the main text). The particle will have a dimensionless momentum $p_f = \gamma_f\beta_f$ ($p_s = \gamma_s\beta_s$) and angle cosine with respect to the shock normal of μ_f (μ_s) in the fluid (NIF) frame. The non-covariant momentum distribution function downstream of the *probability of return plane* located at x (and all positions further downstream) assumes the form

$$f(\vec{\boldsymbol{p}}_f) = \frac{N\delta(p_f - p_0)}{4\pi p_f^2},$$
$$N = \int f(\vec{\boldsymbol{p}}_f)d^3\vec{\boldsymbol{p}}_f \equiv \int f_s(\vec{\boldsymbol{p}}_s)d^3\vec{\boldsymbol{p}}_s. \qquad \text{(A1)}$$

in the local fluid frame. Observe that N, the total number of particles, is a Lorentz invariant under boosts along the shock normal, and f is to be distinguished from the phase space density $f(\vec{\boldsymbol{r}},\ \vec{\boldsymbol{p}})$. Equation (10.2) of Landau & Lifshitz (1975) then gives the transformation of the distribution functions as $\gamma_s f_s(\vec{\boldsymbol{p}}_s) = \gamma_f f_f(\vec{\boldsymbol{p}}_f)$; in covariant formulations, the particle Lorentz factor is absorbed into the definition of f. This is employed in the second integral in Equation (A1), along with the fluid frame distribution function. To integrate over the delta function, it is necessary to change variables $dp_s \rightarrow dp_f$, so that

$$N = 2\pi\int \frac{p_s^2\,dp_s}{\gamma_s}\,\gamma_f\,f_f(\vec{\boldsymbol{p}}_f)\,d\mu_s \equiv \frac{N}{2}\int \frac{\gamma_s\beta_s^2}{\gamma_f\beta_f^2}\left|\frac{\partial p_s}{\partial p_f}\right| d\mu_s. \qquad \text{(A2)}$$

Hereafter, the identity $p_f = p_0$ will be assumed. The partial Jacobian $|\partial p_s/\partial p_f|$ can be determined by first writing the Lorentz boost relations for the particle momentum:

$$p_s\mu_s = \Gamma(\gamma_f\beta + p_f\mu_f)$$
$$p_s\sqrt{1-\mu_s^2} = p_f\sqrt{1-\mu_f^2}. \qquad \text{(A3)}$$

After moderate algebraic manipulation, one can eliminate μ_f and solve for p_s/p_f as a function of p_f and μ_s:

$$\frac{p_s}{p_f} = \frac{\gamma_f}{\Gamma^2}\frac{S+\chi\mu_s}{1-\beta^2\mu_s^2} \quad \text{for} \quad S = \frac{\Gamma}{\gamma_f}\sqrt{1-\chi^2(1-\mu_s^2)},$$
$$\chi = \frac{\Gamma\beta}{\gamma_f\beta_f}. \qquad \text{(A4)}$$

Additionally, holding the integration variable, μ_s, constant, one can derive

$$\left|\frac{\partial p_s}{\partial p_f}\right| = \frac{\Gamma\gamma_s}{S\gamma_f^2}. \qquad \text{(A5)}$$

These allow us to rewrite Equation (A2) in the form

$$N = \int_{-1}^{1}\frac{dN}{d\mu_s}\,d\mu_s,$$
$$\frac{dN}{d\mu_s} = \frac{N\gamma_f}{2\Gamma^3}\frac{(S+\chi\mu_s)^2}{S\left(1-\beta^2\mu_s^2\right)^2}$$
$$= \frac{N\gamma_f}{2\Gamma^3}\frac{d\Sigma}{d\mu_s} \quad \text{for} \quad \Sigma = \frac{\mu_s(S+\chi\mu_s)}{1-\beta^2\mu_s^2}. \qquad \text{(A6)}$$

The angular distribution $dN/d\mu_s$ describes the beaming appearing in the NIF shock frame of an isotropic distribution in the fluid frame of fixed, specified momentum p_f. It is applicable to arbitrary γ_f, not just ultrarelativistic cases $\gamma_f \gg 1$, the usual restricted consideration (e.g., see Peacock 1981). The identity for $dN/d\mu_s$, casting it in terms of a perfect derivative $d\Sigma/d\mu_s$, can be established using a moderate amount of algebra; it nicely facilitates the derivation of the integral identity for N in Equation (A6).

To formulate probabilities of transmission and return at position x, the angular distribution $dN/d\mu_s$ must be weighted by the flux of particles incident upon the plane at x that is parallel to the shock plane. In the NIF, this weighting factor is proportional to the density of particles, which is proportional to γ_s, and also to the velocity component $v_s|\mu_s|$ along the x-direction. In this way, we form *flux angular distributions* using Equation (A4) as follows:

$$\frac{d\mathcal{F}}{d\mu_s} = C\,|\mu_s|\,\frac{(S+\mu_s\chi)^3}{S\left(1-\beta^2\mu_s^2\right)^3} \equiv C\,|\Sigma|\,\frac{d\Sigma}{d\mu_s}, \qquad \text{(A7)}$$

for C being a constant of normalization. This formula generalizes that employed in Peacock (1981), which is restricted to $\gamma_f \gg 1$ cases. It is easily seen that the integrands in Equation (26) of Peacock's paper are proportional to the $\gamma_f \rightarrow \infty$ limit of Equation (A7), and can essentially be derived using light aberration considerations. The total probability P_r of return to x of particles of fixed p_f incident from the upstream side is then the ratio of two integrals over the flux distribution:

$$P_r = \frac{\mathcal{F}_{d\rightarrow u}}{\mathcal{F}_{u\rightarrow d}} = \left(\frac{\beta_f-\beta}{\beta_f+\beta}\right)^2,$$
$$\mathcal{F}_{d\rightarrow u} = \int_{-1}^{0}\frac{d\mathcal{F}}{d\mu_s}\,d\mu_s, \quad \mathcal{F}_{u\rightarrow d} = \int_{0}^{1}\frac{d\mathcal{F}}{d\mu_s}\,d\mu_s. \qquad \text{(A8)}$$

This simple expression for P_r is valid for any flow speed β and any particle speed $\beta_f \geqslant \beta$; it was first derived for non-relativistic shocks (i.e., $\beta \ll 1$) by Bell (1978) and for relativistic shocks with high-speed ($\beta_f \approx 1$) particles by

Peacock (1981). Again, recognizing the appearance of a perfect derivative $d(\Sigma^2)/d\mu_s$ in the flux distributions expedites the integrations in Equation (A8). The direction of the magnetic field and the level of cross-field diffusion are irrelevant to the derivation of the flux angular distribution and probability of return. Technically these formulae, as derived, must be applied in *a downstream NIF*; in practice, for many Rankine–Hugoniot solutions, such as for high Alfvénic Mach numbers (e.g., see, Figures 2 and 3), the flow deflection at the shock is small, and the downstream and upstream NIF frames are almost coincident.

The simulation computes the statistical probability of return to the plane at x according to P_r. Those particles that are deemed to escape are eliminated from the simulation. For those that return, their returning value of $\mu_s \leqslant 0$ is selected randomly from the distribution in Equation (A7) when it is normalized to unity on $-1 \leqslant \mu_s \leqslant 0$. Then, the constant of proportionality is $C = 2\gamma_f^2\beta_f^2/\Gamma^6/(\beta_f - \beta)^2$. Upon return, the particle is placed at x with the same (y, z) coordinates it originally crossed with; the system is uniform in the dimensions transverse to the shock normal, so this step introduces no bias. After μ_s is determined, the phase of the momentum vector about the shock normal is selected randomly from a uniform distribution on $[0, 2\pi]$. The returning particle momentum vector is then totally specified, and is routinely cast in rotated coordinates to identify variables connected to gyration about oblique magnetic fields.

REFERENCES

Abdo, A. A., Ackermann, M., Ajello, M., et al. 2009, ApJ, 707, 1310
Abdo, A. A., Ackermann, M., Ajello, M., et al. 2010, ApJ, 715, 429
Aharonian, F., Akhperjanian, A., Beilicke, M., et al. 2003, A&A, 410, 813
Arfken, G. B., & Weber, H. J. 2001, Mathematical Methods for Physicists (5th ed.; Orlando, FL: Academic)
Armstrong, T. P., Pesses, M. E., & Decker, R. B. 1985, Collisionless Shocks in the Heliosphere: Reviews of Current Research (Washington, DC: American Geophysical Union), 271
Ballard, K. R., & Heavens, A. F. 1991, MNRAS, 251, 438
Baring, M. G. 1999, Proc. 26th ICRC (Salt Lake City), 4, 5
Baring, M. G. 2002, PASA, 19, 60
Baring, M. G. 2004, Nucl. Phys. B, 136, 198
Baring, M. G. 2011, Adv. Space Res., 47, 1427
Baring, M. G., Ellison, D. C., Reynolds, S. P., Grenier, I. A., & Goret, P. 1999, ApJ, 513, 311
Baring, M. G., Ogilvie, K. W., Ellison, D. C., & Forsyth, R. J. 1997, ApJ, 476, 889
Baring, M. G., & Summerlin, E. J. 2007, Ap&SS, 307, 165
Baring, M. G., & Summerlin, E. J. 2009, in AIP Conf. Proc. 1183, Shock Waves in Space and Astrophysical Environments, ed. X. Ao, R. Burrows, & G. P. Zank (Melville, NY: AIP), 74
Bednarz, J., & Ostrowski, M. 1998, Phys. Rev. Lett., 80, 18
Begelman, M. C., & Kirk, J. G. 1990, ApJ, 353, 66
Bell, A. R. 1978, MNRAS, 182, 147
Bell, A. R., Schure, K. M., & Reville, B. 2011, MNRAS, in press
Blandford, R. D., & Eichler, D. 1987, Phys. Rep., 154, 1
Blandford, R. D., & McKee, C. F. 1976, Phys. Fluids, 19, 1130
Blasi, P., & Vietri, M. 2005, ApJ, 626, 877
Blumenthal, G. R. 1971, Phys. Rev. D, 3, 2308
Decker, R. B. 1988, Space Sci. Rev., 48, 195
Decker, R. B., Pesses, M. E., & Krimigis, S. M. 1981, J. Geophys. Res., 86, 819
Decker, R. B., & Vlahos, L. 1986, ApJ, 306, 710
de Hoffmann, F., & Teller, E. 1950, Phys. Rev., 80, 692
Double, G. P., Baring, M. G., Jones, F. C., & Ellison, D. C. 2004, ApJ, 600, 485
Drury, L. O'C. 1983, Rep. Prog. Phys., 46, 973
Ellison, D. C., Baring, M. G., & Jones, F. C. 1995, ApJ, 453, 873
Ellison, D. C., Baring, M. G., & Jones, F. C. 1996, ApJ, 473, 1029
Ellison, D. C., & Double, G. P. 2002, Astropart. Phys., 18, 213
Ellison, D. C., & Double, G. P. 2004, Astropart. Phys., 22, 323
Ellison, D. C., & Eichler, D. 1984, ApJ, 286, 691
Ellison, D. C., Jones, F. C., & Baring, M. G. 1999, ApJ, 512, 403
Ellison, D. C., Jones, F. C., & Eichler, D. 1981, J. Geophys., 50, 110
Ellison, D. C., Jones, F. C., & Reynolds, S. P. 1990a, ApJ, 360, 702
Ellison, D. C., Möbius, E., & Paschmann, G. 1990b, ApJ, 352, 376
Forman, M. A., Jokipii, J. R., & Owens, A. J. 1974, ApJ, 192, 535
Gallant, Y. A., Hoshino, M., Langdon, A. B., Arons, J., & Max, C. E. 1992, ApJ, 391, 73
Garcia, A. L. 2000, Numerical Methods for Physics (2nd ed.; Upper Saddle River, NJ: Prentice-Hall)
Garson, A. B., Baring, M. G., & Krawczynski, H. 2010, ApJ, 722, 358
Gerbig, D., & Schlickeiser, R. 2011, ApJ, 733, 32
Giacalone, J., Burgess, D., & Schwartz, S. J. 1992, in Study of the Solar-Terrestrial System, ed. J. J. Hunt (ESA-SP 346; Noordwijk: ESA), 65
Gosling, J. T., Thomsen, M. F., Bame, S. J., & Russell, C. T. 1989, J. Geophys. Res., 94, 3555
Hartman, R. C., Bertsch, D. L., Fichtel, C. E., et al. 1992, ApJ, 385, L1
Heavens, A. F., & Drury, L. O'C. 1988, MNRAS, 235, 997
Hededal, C. B., Haugbolle, T., Frederiksen, J. T., & Nordlund, A 2004, ApJ, 617, L107
Jokipii, J. R. 1982, ApJ, 255, 716
Jones, F. C. 1978, ApJ, 222, 1097
Jones, F. C., & Ellison, D. C. 1991, Space Sci. Rev., 58, 259
Kirk, J. G., Guthmann, A. W., Gallant, Y. A., & Achterberg, A. 2000, ApJ, 542, 235
Kirk, J. G., & Heavens, A. F. 1989, MNRAS, 239, 995
Kirk, J. G., & Schneider, P. 1987, ApJ, 315, 425
Krennrich, F., Bond, I. H., Bradbury, S. M., et al. 2002, ApJ, 575, L9
Landau, L. D., & Lifshitz, E. M. 1975, The Classical Theory of Fields (4th ed.; Oxford: Butterworth-Heinemann)
Lee, M. A. 1983, J. Geophys. Res., 88, 6109
Lee, M. A. 1984, Adv. Space Res., 4, 295
Liang, E. P., & Nishimura, K. 2004, Phys. Rev. Lett., 92, 5005
Mason, G. M., Gloeckler, G., & Hovestadt, D. 1983, ApJ, 267, 844
Medvedev, M. V., Fiore, M., Fonseca, R. A., Silva, L. O., & Mori, W. B. 2005, ApJ, 618, L75
Mészáros, P. 2001, Science, 291, 79
Möbius, E., Scholer, M., Sckopke, N., Paschmann, G., & Luehr, H. 1987, Geophys. Res. Lett., 14, 681
Morlino, G., Blasi, P., & Vietri, M. 2007, ApJ, 658, 1069
Niemiec, J., & Ostrowski, M. 2004, ApJ, 610, 851
Niemiec, J., & Ostrowski, M. 2006, ApJ, 641, 984
Nishikawa, K.-I., Hardee, P., Richardson, G., et al. 2005, ApJ, 622, 927
Ostrowski, M. 1991, MNRAS, 249, 551
Peacock, J. A. 1981, MNRAS, 196, 135
Pesses, M. E., & Decker, R. B. 1986, J. Geophys. Res., 91, 4143
Pesses, M. E., Decker, R. B., & Armstrong, T. P. 1982, Space Sci. Rev., 32, 185
Piran, T. 1999, Phys. Rep., 314, 575
Pryadko, J. M., & Petrosian, V. 1997, ApJ, 482, 774
Punch, M., Akerlof, C. W., Cawley, M. F., et al. 1992, Nature, 358, 477
Rybicki, G. B., & Lightman, A. P. 1979, Radiative Processes in Astrophysics (New York: Wiley)
Sarris, E. T., & Van Allen, J. A. 1974, J. Geophys. Res., 79, 4157
Scholer, M., Hovestadt, D., Ipavich, F. M., & Gloeckler, G. 1980, J. Geophys. Res., 85, 4602
Silva, L. O., Fonseca, R. A., Tonge, J. W., et al. 2003, ApJ, 596, L121
Sironi, L., & Spitkovsky, A. 2011, ApJ, 726, 75
Smolsky, M. V., & Usov, V. V. 1996, ApJ, 461, 858
Spitkovsky, A. 2008, ApJ, 682, L5
Stecker, F. W., Baring, M. G., & Summerlin, E. J. 2007, ApJ, 667, L29
Stoer, J., & Bulirsch, R. 1980, Introduction to Numerical Analysis (New York: Springer), Chap. 7.2.14
Summerlin, E. J., & Baring, M. G. 2006, Adv. Space Res., 37, 1426
Synge, J. L. 1957, The Relativistic Gas (Amsterdam: North Holland)
Tan, L. C., Mason, G. M., Gloeckler, G., & Ipavich, F. M. 1988, J. Geophys. Res., 93, 7225
Terasawa, T. 1979, Planet. Space Sci., 27, 193
Vandas, M. 2001, J. Geophys. Res., 106, 1859
Webb, G. M., Axford, W. I., & Terasawa, T. 1983, ApJ, 270, 537